

Influence of the Galactic bar on the kinematics of the disc stars with *Gaia* EDR3 data

A. M. Melnik,^{1*} A. K. Dambis,¹ E. N. Podzolkova² and L. N. Berdnikov¹

¹*Sternberg Astronomical Institute, Lomonosov Moscow State University, Universitetskii pr. 13, Moscow, 119991 Russia*

²*Faculty of Physics, Lomonosov Moscow State University, Leninskie Gory 1-2, Moscow, 119991 Russia*

Accepted 2021 July 13. Received 2021 June 14; in original form 2021 January 27

ABSTRACT

A model of the Galaxy with the outer ring R_1R_2 can explain the observed distribution of the radial, V_R , and azimuthal, V_T , velocity components along the Galactocentric distance, R , derived from the *Gaia* EDR3 data. We selected stars from the *Gaia* EDR3 catalogue with reliable parallaxes, proper motions, and line-of-sight velocities lying near the Galactic plane, $|z| < 200$ pc, and in the sector of the Galactocentric angles $|\theta| < 15^\circ$ and calculated the median velocities V_R and V_T in small bins along the distance R . The distribution of observed velocities appears to have some specific features: the radial velocity V_R demonstrates a smooth fall from $+5$ km s⁻¹ at the distance of $R \approx R_0 - 1.5$ kpc to -3 km s⁻¹ at $R \approx R_0 + 1.0$ kpc while the azimuthal velocity V_T shows a sharp drop by 7 km s⁻¹ in the distance interval $R_0 < R < R_0 + 1.0$ kpc, where R_0 is the solar Galactocentric distance. We build a model of the Galaxy including bulge, bar, disc, and halo components, which reproduces the observed specific features of the velocity distribution in the Galactocentric distance interval $|R - R_0| < 1.5$ kpc. The best agreement corresponds to the time 1.8 ± 0.5 Gyr after the start of the simulation. A model of the Galaxy with the bar rotating at the angular velocity of $\Omega_b = 55 \pm 3$ km s⁻¹ kpc⁻¹, which sets the OLR of the bar at the distance of $R_0 - 0.5 \pm 0.4$ kpc, provides the best agreement between the model and observed velocities. The position angle of the bar, θ_b , corresponding to the best agreement between the model and observed velocities is $\theta_b = 45 \pm 15^\circ$.

Key words: Galaxy: kinematics and dynamics – galaxies: bar.

1 INTRODUCTION

Bars were found in nearly 70 percent of bright disc galaxies (Eskridge et al. 2000; Menéndez-Delmestre et al. 2007). On the whole, the fraction of barred galaxies increases with decreasing redshift, but during the last ~ 4 Gyr, the fraction of barred galaxies changes negligibly (Sheth et al. 2008; Melvin, Masters & the Galaxy Zoo Team 2013). In many cases the formation of a bar does not require an external perturbation but results from the secular evolution of galaxies (Kormendy & Kennicutt 2004).

There are a lot of data indicating the presence of the bar in the Galaxy. The gas kinematics (Pohl, Englmaier & Bissantz 2008; Gerhard 2011; Pettitt et al. 2014), infrared observations (Dwek et al. 1995; Benjamin et al. 2005; Cabrera-Lavers et al. 2007; Churchwell et al. 2009; González-Fernández et al. 2012), as well as the X-shaped distribution of red giants in the central part of the disc (Li & Shen 2012; Ness & Lang 2016; Simion et al. 2017) confirm the presence of a bar in the Galaxy. Estimates of the length of the bar semimajor axis and its angular velocity lie in the range $a = 3\text{--}5$ kpc and $\Omega_b = 30\text{--}60$ km s⁻¹ kpc⁻¹, respectively. The position angle of the bar with respect to the Sun is supposed to be $\theta_b = 15\text{--}45^\circ$, implying that the end of the bar that is nearest to the Sun is located in quadrant I.

The age of the Galactic bar is a subject of scientific debates (Haywood et al. 2016; Nataf 2016; Bensby et al. 2017; Bernard et al. 2017; Carrillo et al. 2019; Fujii et al. 2019). Here we consider

a strong bar rotating with a constant angular velocity, though oval structures existed in the Galactic disc much earlier. The presence of young metal-rich stars in the Galactic disc at the distances of $R = 2\text{--}3$ kpc from the centre supports the idea that the Galactic bar formed 2–3 Gyr ago (Debattista et al. 2019; Baba & Kawata 2020; Hasselquist et al. 2020, and other papers).

The locations of the Outer and Inner Lindblad Resonances of the bar are determined by the ratio of the difference between the angular velocity of the bar and the disc ($\Omega - \Omega_b$) to the frequency of the epicyclic motion κ :

$$\frac{\kappa}{\Omega - \Omega_b} = \pm 2/1, \quad (1)$$

where $-2/1$ corresponds to the Outer Lindblad Resonance (OLR), but $+2/1$ – to the Inner Lindblad Resonance (ILR). Besides, resonances of order $\pm 4/1$ are also important (Contopoulos & Papayannopoulos 1980; Contopoulos & Grosbol 1989; Athanassoula 1992).

The resonance between the orbital rotation with respect to the bar and the epicyclic motion causes the formation of elliptic resonance rings. There are three types of resonance rings: nuclear (n), inner (r) and outer (R_1 and R_2) rings. The nuclear rings lie near the ILR and are stretched perpendicular to the bar; the inner rings form near the inner $4/1$ resonance and are oriented along the bar; the outer rings R_1 and R_2 are located near the OLR: the rings R_1 or pseudo-rings R'_1 (broken rings) lie a bit closer to the galactic centre and are stretched perpendicular to the bar while the rings R_2 or pseudo-rings R'_2 are located a bit farther away from the centre and are stretched parallel to the bar. There is also a mixed morphological type $R_1R'_2$ including

* E-mail: anna@sai.msu.ru

both R_1 and R'_2 outer rings/pseudorings (Buta & Crocker 1991; Buta 1995; Buta & Combes 1996; Rodriguez-Fernandez & Combes 2008; Sormani et al. 2018). The fraction of galaxies with outer rings is as high as 20–30 per cent among galaxies with strong and moderate bars (Cameron et al. 2014).

The backbone of resonance rings is stable direct periodic orbits which are followed by numerous quasi-periodic orbits. There are two basic families of stable direct periodic orbits, x_1 and x_2 . Orbits of the x_1 family support the bar inside the corotation radius. Orbits of the x_2 family are elongated perpendicular to the bar and support the nuclear rings between two ILRs. Near the OLR of the bar the main family of periodic orbits x_1 splits into two families: $x_1(1)$ and $x_1(2)$. The main stable periodic orbits $x_1(2)$ lying between the $-4/1$ and $-2/1$ (OLR) resonances are elongated perpendicular to the bar while the orbits $x_1(1)$ located outside the OLR are stretched along the bar. The periodic orbits $x_1(2)$ support the outer rings R_1 while the orbits $x_1(1)$ support the outer rings R_2 (Contopoulos & Papayannopoulos 1980; Schwarz 1981; Contopoulos & Grosbol 1989; Buta & Combes 1996).

Athanassoula, Romero-Gómez & Masdemont (2009) studied manifold tubes emanating from the unstable Lagrangian points located near the ends of the bar. They showed that less strong bars give rise to R_1 rings/pseudo-rings, while stronger bars drive spirals, R_2 and R_1R_2 rings/pseudo-rings.

The bimodal velocity distribution of disc stars in the solar neighbourhood can be explained by the location of the Sun near the OLR of the bar (Kalnajs 1991; Dehnen 2000; Fux 2001; Fragkoudi et al. 2019; Sanders, Smith & Evans 2019; Asano et al. 2020; Chiba, Friske & Schonrich 2021; Trick et al. 2021, and other papers). Furthermore, galaxies with a flat rotation curve and a fast bar, which ends near the corotation radius (Debattista & Sellwood 2000; Rautiainen, Salo & Laurikainen 2008), produce an OLR at a distance nearly twice exceeding the length of the bar semimajor axis, $R \approx 2a$. For the Galaxy, this distance nearly corresponds to the solar Galactocentric distance, R_0 .

Modelling of the outer rings shows that they form 0.5–1.0 Gyr after the bar is turned on. The ring R_1 appears first while the ring R_2 forms a bit later, ~ 1 Gyr after the start of the simulation (Schwarz 1981; Byrd et al. 1994; Rautiainen & Salo 1999, 2000). Rautiainen & Salo (2000) studied the outer ring morphology in N-body models and found cyclic changes in the ring type: from $R_1R'_2$ to R'_2 and back to $R_1R'_2$.

Models with analytical bars are of particular interest in studies of the kinematics of Galactic stars. Melnik & Rautiainen (2009) showed that a model of the Galaxy with a two-component outer ring $R_1R'_2$ can explain the average velocities of young stars in the Sagittarius and Perseus star–gas complexes (Efremov & Sitnik 1988). Melnik (2019) found that a model of the Galaxy with a bar rotating with the angular velocity of $\Omega_b = 50 \pm 2 \text{ km s}^{-1} \text{ kpc}^{-1}$ can reproduce the average velocities of young stars in three star–gas complexes: Sagittarius, Perseus, and Local System. The Sagittarius complex with the average radial velocity, $V_R = +7.5 \pm 2.1 \text{ km s}^{-1}$, directed away from the Galactic centre belongs to the ring R_1 while the Perseus complex with the radial velocity, $V_R = -4.7 \pm 2.2 \text{ km s}^{-1}$, directed towards the Galactic centre is associated with the ring R_2 . The Local System is located between these two complexes and has the average radial velocity of $V_R = +5.4 \pm 2.6 \text{ km s}^{-1}$. The model considered can reproduce the velocity in the Local System during the time period 1–2 Gyr after the start of modelling. The best agreement with observations corresponds to the position angle of the bar lying in the range $\theta_b = 40^\circ\text{--}52^\circ$.

Rautiainen & Melnik (2010) built an N-body model of the Galaxy which demonstrates the formation of a bar and outer rings. The velocities of model particles were averaged over 1 Gyr time periods

for comparison with observations. Such averaging suppresses the influence of slow modes and random velocity changes. The average model velocities in N-body models reproduce the observed velocities of young stars in the Sagittarius, Perseus, and Local System star–gas complexes.

The kinematics and distribution of classical Cepheids, OB associations, and young star clusters in the 3-kpc solar neighbourhood are indicative of the presence of ‘the tuning-fork-like’ structure in the Galactic disc, which can be accounted for by the existence of two segments of the outer rings fusing together near the Carina star–gas complex (Melnik et al. 2015, 2016). In addition, models of the Galaxy with a two-component outer ring $R_1R'_2$ can reproduce the location of the Carina–Sagittarius spiral arm, where the Carina arm is located near the segment of the outer ring R_2 while the Sagittarius arm lies near the ring R_1 (Melnik & Rautiainen 2011).

The early installment of the third *Gaia* data release (*Gaia* EDR3) including proper motions and parallaxes for 1.5 billion stars opens new possibilities for the study of the Galactic structure and kinematics. *Gaia* EDR3 also lists 7.2 million stellar line-of-sight velocities presented by the second *Gaia* data release (*Gaia* DR2) and adopted by *Gaia* EDR3 with some small corrections (Gaia Collaboration 2016, 2018a, c, 2020; Lindegren et al. 2020).

In this paper, we study the kinematics of Galactic stars with the *Gaia* EDR3 data and build a model of the Galaxy which reproduces the observed distributions of the radial and azimuthal velocities along the Galactocentric distance. Section 2 describes the observational data. Section 3 presents the dynamical model of the Galaxy. Section 4 describes the results: a comparison of the observed and model velocities and velocity dispersions, the search for the optimal values of the bar angular velocity, Ω_b , and the positional angle of the bar, θ_b . The discussion and main conclusions are given in Section 5.

2 OBSERVATIONAL DATA

The average accuracy of proper motions and parallaxes of the *Gaia* EDR3 catalogue allows the velocities and distances to stars located within 1 kpc from the Sun to be derived with the average error of $\pm 0.2 \text{ km s}^{-1}$ and $\pm 50 \text{ pc}$, respectively. The average accuracy of *Gaia* EDR3 line-of-sight velocities is $\pm 2 \text{ km s}^{-1}$ (Gaia Collaboration 2018a, 2020).

We selected *Gaia* EDR3 stars located near the Galactic plane, $|z| < 200 \text{ pc}$, and in the sector of the Galactocentric angles $|\theta| < 15^\circ$ that have parallaxes, ϖ , determined with the relative error less than 20 per cent ($\varpi/\varepsilon_\varpi > 5$) and line-of-sight velocities measured by the *Gaia* spectrometer. We excluded from the initial sample of *Gaia* EDR3 stars (2886715 stars) 493 472 objects (17 per cent) with the re-normalized error (RUWE) greater than $\text{RUWE} > 1.4$ (Lindegren et al. 2018). The final sample of *Gaia* EDR3 stars includes 2393 243 objects. The heliocentric distances to stars were derived from *Gaia* EDR3 parallaxes without any zero-point correction: $r = 1/\varpi$.

We also compared observational distributions derived from the *Gaia* EDR3 and *Gaia* DR2 data. The initial sample of *Gaia* DR2 stars lying near the Galactic plane, $|z| < 200 \text{ pc}$, and in the sector of the Galactocentric angles $|\theta| < 15^\circ$ that have reliable parallaxes and known line-of-sight velocities includes 2987 601 objects. We excluded from the initial sample 243 059 stars (8.1 per cent) with the re-normalized error $\text{RUWE} > 1.4$ and 75504 stars (2.5 per cent) with the number of visibility periods $n_{\text{vis}} \leq 8$. The heliocentric distances, r , were derived from *Gaia* DR2 parallaxes, ϖ , in the following way:

$$r = \frac{1}{\varpi - \Delta\varpi}, \quad (2)$$

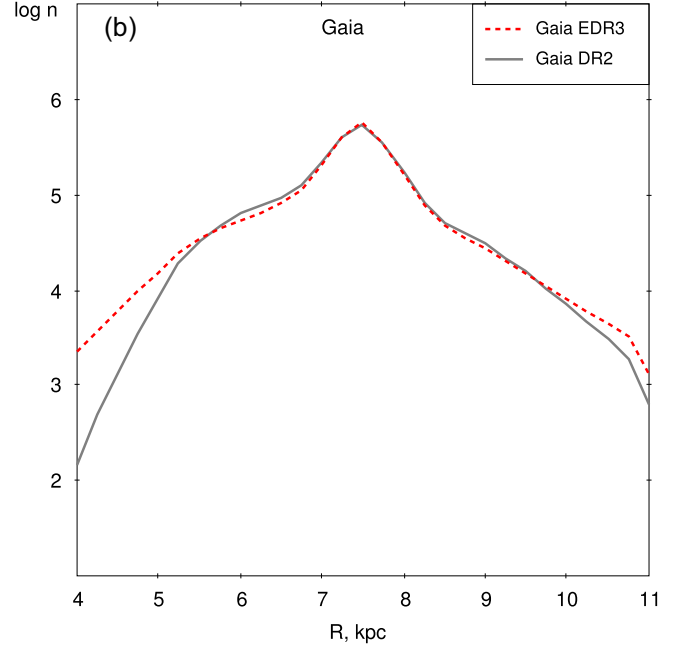
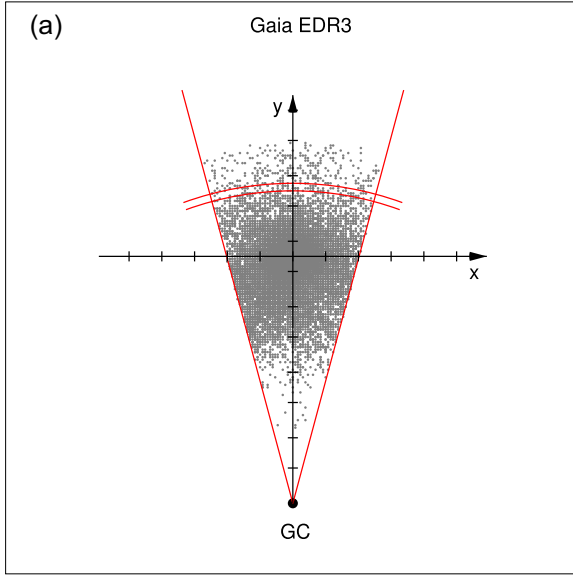


Figure 1. (a) Distribution of *Gaia* EDR3 stars located near the Galactic plane, $|z| < 200$ pc, and in the sector of the Galactocentric angles $|\theta| < 15^\circ$ (grey points). We selected *Gaia* EDR3 stars with reliable parallaxes, known proper motions and line-of-sight velocities. Only 1 per cent of objects are shown. For an example, we outlined one $\Delta R = 250$ -pc wide bin by two arcs. The Galactic centre (GC) is at the bottom, the axes x and y are directed toward the Galactic rotation and away from the Galactic centre, respectively; the Sun is at the origin. (b) Logarithmic dependence of the numbers of stars, n , in 250-pc wide bins on the distance R derived from the *Gaia* EDR3 and *Gaia* DR2 data.

where $\Delta\varpi$ is a parallax zero-point offset. The value of the offset $\Delta\varpi$ depends on the magnitude G : the brighter the star, the larger the absolute value of $\Delta\varpi$. For stars with $G = 8^m$ the offset $\Delta\varpi$ attains the value of -0.120 mas while for quasars it is only $\Delta\varpi = -0.030$ mas (Arenou et al. 2018; Lindegren et al. 2018; Melnik & Dambis 2020). We excluded stars with the magnitude $G < 10^m$ (220 710 stars) and adopted for all *Gaia* DR2 stars the parallax zero-point offset of $\Delta\varpi = -0.05$ mas (Riess et al. 2018; Yalvalieva et al. 2018; Leung & Bovy 2019; Schönrich, McMillan & Eyer 2019; Zinn et al. 2019). The final sample of *Gaia* DR2 stars includes 2448 328 objects.

Fig. 1(a) shows the observational sample of stars selected from the *Gaia* EDR3 catalogue. The distribution of stars along the Galactocentric distance R was subdivided into 250-pc wide bins. Fig. 1(b) shows the number of stars, n , in bins at different distances R calculated for the *Gaia* EDR3 and *Gaia* DR2 catalogues. We can see that the *Gaia* EDR3 catalogue includes considerably more stars in the distance interval $R = 4$ –5 kpc than the *Gaia* DR2 catalogue.

We adopted the solar Galactocentric distance to be of $R_0 = 7.5$ kpc (Glushkova et al. 1998; Nikiforov 2004; Feast et al. 2008; Groenewegen, Udalski & Bono 2008; Reid et al. 2009; Dambis et al. 2013; Francis & Anderson 2014; Boehle et al. 2016; Branham 2017). On the whole, the choice of the value of R_0 in the range 7–9 has virtually no effect on the results.

The velocity components of the Sun in the Galactic centre rest frame in the directions towards the Galactic rotation, V_{T0} , towards the Galactic centre, V_{R0} , and in the direction perpendicular to the Galactic plane, V_{Z0} , are adopted to be $V_{T0} = \Omega_0 R_0 + 12.0$ km s $^{-1}$, $V_{R0} = 10.0$ km s $^{-1}$, and $V_{Z0} = 7.0$ km s $^{-1}$, where Ω_0 is the angular velocity of the rotation of the Galactic disc at the solar distance R_0 and its value is taken to be $\Omega_0 = 30.0$ km s $^{-1}$ kpc $^{-1}$. The adopted Ω_0 , V_{T0} , V_{R0} , and V_{Z0} are consistent with values derived from an analysis of the kinematics of OB associations with the *Gaia* DR2 data (Melnik & Dambis 2020).

The velocities of stars in the radial, V_R , and azimuthal, V_T , directions as well as in the direction perpendicular to the Galactic plane, V_Z , are computed in the following way:

$$V_R = (V_r \cos b - V_b \sin b) \sin \alpha + V_l \cos \alpha + V_{T0} \sin \theta - V_{R0} \cos \theta, \quad (3)$$

$$V_T = (V_r \cos b - V_b \sin b) \cos \alpha - V_l \sin \alpha + V_{T0} \cos \theta + V_{R0} \sin \theta, \quad (4)$$

$$V_Z = V_r \sin b + V_b \cos b + V_{Z0}, \quad (5)$$

where the angle α is:

$$\alpha = \ell + \theta - \pi/2 \quad (6)$$

and V_r is the line-of-sight velocity. The stellar velocities along the Galactic longitude V_l and latitude V_b are determined from the relations:

$$V_l = 4.74 \mu_l r, \quad (7)$$

$$V_b = 4.74 \mu_b r, \quad (8)$$

where μ_l and μ_b are *Gaia* proper motions along the Galactic longitude and latitude, respectively. The factor $4.74 \times r$ (kpc) transforms units of mas yr $^{-1}$ into km s $^{-1}$.

Fig. 2 (left-hand panel) shows the variations in the median velocities, V_R , V_T , and V_Z , with the Galactocentric distance, R , derived from the *Gaia* EDR3 and *Gaia* DR2 data. The median velocities are calculated in $\Delta R = 250$ -pc wide bins. The average errors in the determination of the median *Gaia* EDR3 velocities V_R , V_T , and V_Z in bins at the interval $R = 5$ –10 kpc are 0.16, 0.11, and 0.07 km s $^{-1}$, respectively.

Fig. 2(a) shows that the radial velocity V_R reaches a maximum of $+5$ km s $^{-1}$ at the distance of $R \sim 6$ kpc and a minimum of

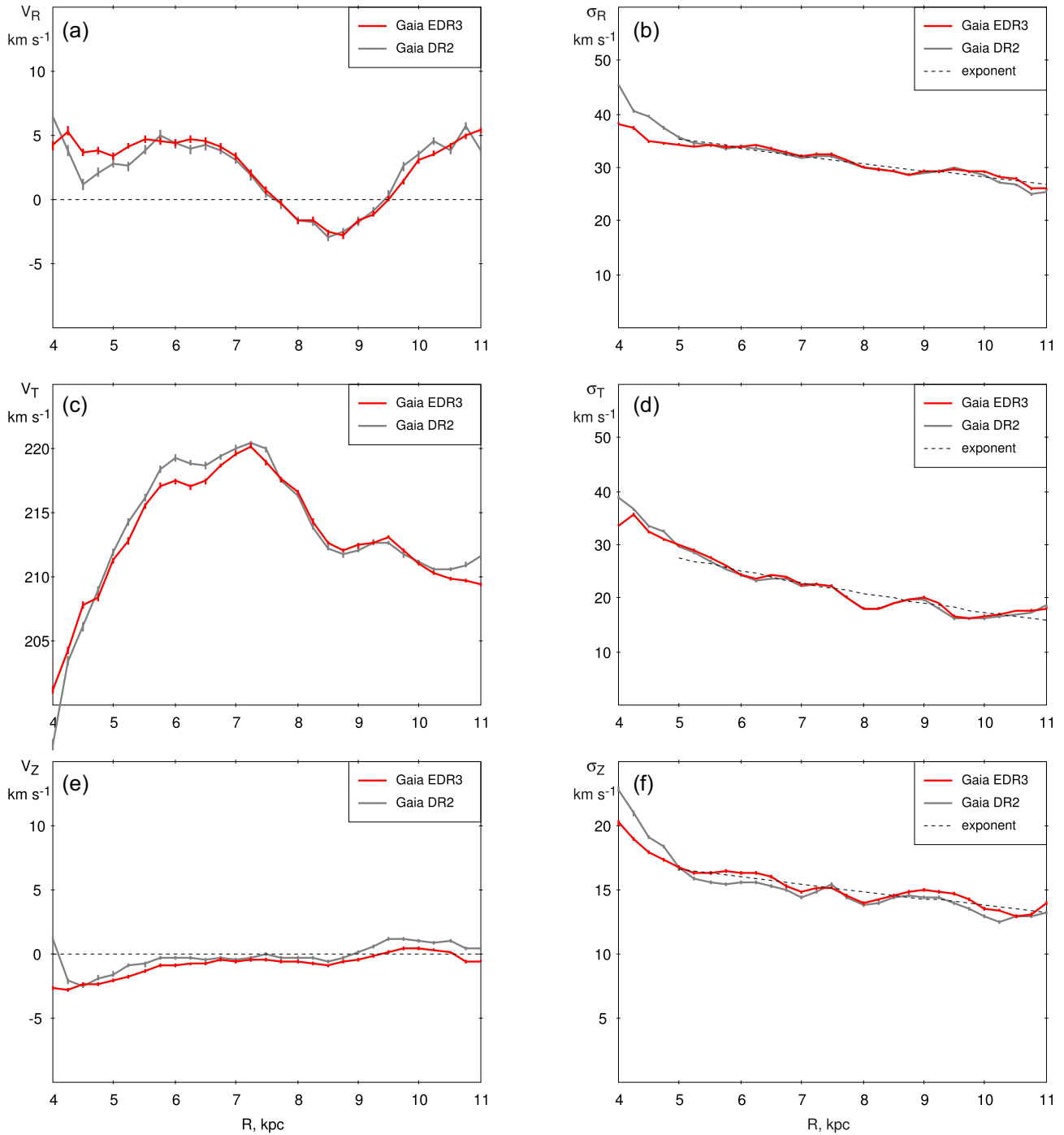


Figure 2. Variations in the velocity components, V_R , V_T , and V_Z (left-hand panel), and in the velocity dispersions, σ_R , σ_T , and σ_Z (right-hand panel), along the Galactocentric distance, R , derived from the *Gaia* EDR3 and *Gaia* DR2 data. The median velocities are calculated in 250-pc wide bins. The vertical lines on the curves demonstrate the random errors in the determination of the velocities and velocity dispersions. We can see (a) that the radial velocity V_R reaches a maximum of $+5 \text{ km s}^{-1}$ at the distance of $R \sim 6 \text{ kpc}$ and a minimum of $V_R \sim -3 \text{ km s}^{-1}$ at $R \sim 8.5 \text{ kpc}$. Note also that the V_R -profile derived from the *Gaia* DR3 data is flatter in the distance interval 4–6 kpc than the profile derived from the *Gaia* DR2 catalogue. (c) The profile of the azimuthal velocity V_T demonstrates a sharp drop by $\Delta V_T = 7 \text{ km s}^{-1}$ in the distance interval $R = 7.0\text{--}8.5 \text{ kpc}$. Noticeably lower velocities V_T in the distance range 4.0–5.5 kpc can be due to the lack of thin-disc stars in this region. (e) The vertical velocity V_Z remains within $\pm 1 \text{ km s}^{-1}$ in the distance interval 6.0–9.0 kpc but exhibits a velocity bend at the larger distances from the Sun, which can be due to the wrong distance scale. (b, d, f) The variations in the velocity dispersions, σ_R , σ_T , and σ_Z , with the distance R were approximated by the exponential law (the dashed lines).

$V_R \sim -3 \text{ km s}^{-1}$ at $R \sim 8.5 \text{ kpc}$. We can also see that the V_R -profile derived from the *Gaia* DR3 data is flatter in the distance interval 4–6 kpc than the profile derived from the *Gaia* DR2 data.

Fig. 2(c) shows a sharp drop of the azimuthal velocity, V_T , by $\Delta V_T = 7 \text{ km s}^{-1}$ in the distance interval $R = 7.0\text{--}8.5 \text{ kpc}$. We can also see noticeably lower velocities V_T in the distance interval $R = 4.0\text{--}5.5 \text{ kpc}$, which can be due to the lack of thin-disc stars in this

Table 1. Parameters derived from EDR3 data.

$C_R = 44.0 \pm 1.0 \text{ km s}^{-1}$	$S_R = 22.3 \pm 1.4 \text{ kpc}$
$C_T = 43.8 \pm 2.8 \text{ km s}^{-1}$	$S_T = 10.8 \pm 0.9 \text{ kpc}$
$C_Z = 20.0 \pm 0.6 \text{ km s}^{-1}$	$S_Z = 26.9 \pm 2.6 \text{ kpc}$

region. The extinction in the middle of the Galactic plane grows very rapidly in the direction towards the Galactic centre (Neckel & Klare 1980; Marshall et al. 2006; Melnik et al. 2016), so our sample of *Gaia* stars at the distances of $R = 4.0\text{--}5.5$ kpc can contain a larger fraction of stars associated with the thick disc and halo than in other regions. The sources for which a line-of-sight velocity is listed in the *Gaia* DR2 and EDR3 catalogues mostly have the magnitude brighter than $G = 13^m$. So the fraction of thin and thick disc stars as well as the proportion of young versus old stars must depend on the place in the Galactic disc (Gaia Collaboration 2018a, c; Sartoretti et al. 2018; Katz et al. 2019).

Fig. 2(e) shows that the vertical velocity V_Z does not exceed $\pm 1 \text{ km s}^{-1}$ in the distance interval 6.0–9.0 kpc but demonstrates the velocity bend at greater heliocentric distances: V_Z is negative ($V_Z = -2.0 \pm 0.1 \text{ km s}^{-1}$) in the distance interval of $R = 4.0\text{--}5.0$ kpc and positive ($V_Z = +0.5 \pm 0.1 \text{ km s}^{-1}$) at $R = 10.0$ kpc. Generally, the V_Z -velocity bend can be due to two circumstances: wrong distance scale at large heliocentric distances, $r > 2$ kpc, plus some ripple of the Galactic disc. The preponderance of objects at negative or positive Galactic latitudes (the ripple) produces some excess in the average value of the term $V_r \sin b$ (equation 5), which can be uncompensated by the term $V_b \cos b$ due to the distance-scale errors, because V_b is directly proportional to the heliocentric distance r (equation 5 and 8, see also discussion in Melnik & Dambis 2020).

Fig. 2 (right-hand panel) shows the distributions of the velocity dispersions in the radial, azimuthal, and vertical directions, σ_R , σ_T , and σ_Z , along the Galactocentric distance, R , derived from the *Gaia* EDR3 and *Gaia* DR2 data. The median velocity dispersion in each bin was determined as half of the central velocity interval including 68 per cent of objects. We approximated the variations in the velocity dispersions with the distance R by the exponential law and obtained the following dependence for the *Gaia* EDR3 data in the distance interval $R = 5\text{--}11$ kpc:

$$\sigma_R = C_R \exp^{-\frac{R}{S_R}}, \quad (9)$$

$$\sigma_T = C_T \exp^{-\frac{R}{S_T}}, \quad (10)$$

$$\sigma_Z = C_Z \exp^{-\frac{R}{S_Z}}, \quad (11)$$

where the values of the parameters and their errors are listed in Table 1. Note that our estimate of the scale length $S_R = 22.3 \pm 1.4$ kpc is consistent with the value calculated by Eilers et al. (2019), $S_R = 21$ kpc. The characteristic scales derived from the *Gaia* DR2 catalogue ($S_R = 19.9 \pm 1.1$ kpc, $S_T = 10.7 \pm 0.9$ kpc, and $S_Z = 26.4 \pm 2.4$ kpc) agree with the scale lengths calculated for the *Gaia* EDR3 data. Such a large difference between the values of S_R and S_T can be due to systematic effects. The space distribution of stars in our sample (Fig. 1a) suggests that the dispersion of radial velocities, σ_R , is mainly determined by line-of-sight velocities while those of azimuthal velocities, σ_T , is mostly determined by proper motions and parallaxes, which are subject to systematic effects to a greater extent.

The dispersion of radial velocities σ_R at the solar distance amounts to $\sigma_R = 32.5 \text{ km s}^{-1}$ while the value derived from the smoothed distribution (equation 9) is $\sigma_R = 31.5 \text{ km s}^{-1}$.

The root-mean-square deviations between the median velocities in bins derived from the *Gaia* DR2 data and from *Gaia* EDR3 data in the distance interval 5.5–9.5 kpc amount to 0.4, 0.9, and 0.5 km s^{-1} for the components V_R , V_T , and V_Z , respectively.

3 MODEL

3.1 General remarks

In the previous section, we showed that there are no conspicuous systematic motions in the direction perpendicular to the Galactic disc in the vicinity of $|R - R_0| < 1.5$ kpc from the Sun. So the motions in the Galactic plane and in the vertical direction can be thought to be independent, which gives us a possibility to consider a 2D model of the Galaxy.

We built a model of the Galaxy that includes the bulge, bar, exponential disc, and halo. The bar is modelled as a Ferrers ellipsoid with the volume-density distribution ρ defined as follows:

$$\rho = \begin{cases} \rho_0 (1 - \xi^2)^n, & \xi \leq 1 \\ 0, & \xi > 1, \end{cases} \quad (12)$$

where ρ_0 is the central density, ξ equals $\xi^2 = x^2/a^2 + y^2/b^2$ but a and b are the lengths of the major and minor semi-axes of the bar, respectively. The exponent n is adopted to be $n = 2$. The mass of the bar M_b and the central density ρ_0 are related by the expression:

$$M_b = \rho_0 \frac{32\pi ab^2}{105} \quad (13)$$

(Freeman 1970; Athanassoula et al. 1983; Pfenniger 1984; Sellwood & Wilkinson 1993; Binney & Tremaine 2008).

The main model requirement is that the model must reproduce the observed profiles of the radial, V_R , and azimuthal, V_T , velocities as well as the profiles of the velocity dispersions, σ_R and σ_T (Fig. 2). In addition, the model rotation curve must be flat on the Galactic periphery and have the angular velocity of $\Omega_0 = 30 \text{ km s}^{-1} \text{ kpc}^{-1}$ at the solar distance, which agrees with observations and corresponds to the solar azimuthal velocity $V_{T0} = \Omega_0 R_0 + 12 \text{ km s}^{-1}$ used for calculations of stellar velocities with respect to the Galactic centre (Section 2).

We adopted the simulation time to be $T = 3$ Gyr. The model includes $N = 10^7$ particles that simulate the motion of stars in the Galactic disc. This number is enough to produce the velocity profiles with an accuracy comparable to the observational one.

Fig. 3(a) shows the contribution of the bulge, bar, disc, and halo to the total rotation curve. The total rotation curve is practically flat on the periphery and corresponds to the angular velocity of the disc rotation at the solar distance equal to $\Omega_0 = 30.0 \text{ km s}^{-1} \text{ kpc}^{-1}$.

Fig. 3(b) shows the dependence of the angular velocities Ω , $\Omega \pm \kappa/2$, and $\Omega \pm \kappa/4$ on Galactocentric distance R . The horizontal line indicates the angular velocity of the bar, and its intersections with the curves of angular velocities mark the locations of the resonances.

Table 2 lists the model parameters of the bar, bulge, disc, and halo. The semimajor and semiminor axes of the bar are adopted to be $a = 3.5$ and $b = 1.35$ kpc, respectively. The mass of the bar is $1.2 \times 10^{10} M_\odot$. The angular velocity of the bar is taken to be $\Omega_b = 55 \text{ km s}^{-1} \text{ kpc}^{-1}$, which corresponds to the location of the corotation radius ($\Omega = \Omega_b$) and the OLR of the bar at the distances of $R_{\text{CR}} = 4.04$ kpc and $R_{\text{OLR}} = 7.00$ kpc, respectively. The model also includes two Inner Lindblad Resonances (ILRs) located at the distances of $R_{\text{ILRI}} = 0.14$ and $R_{\text{ILRO}} = 0.87$ kpc.

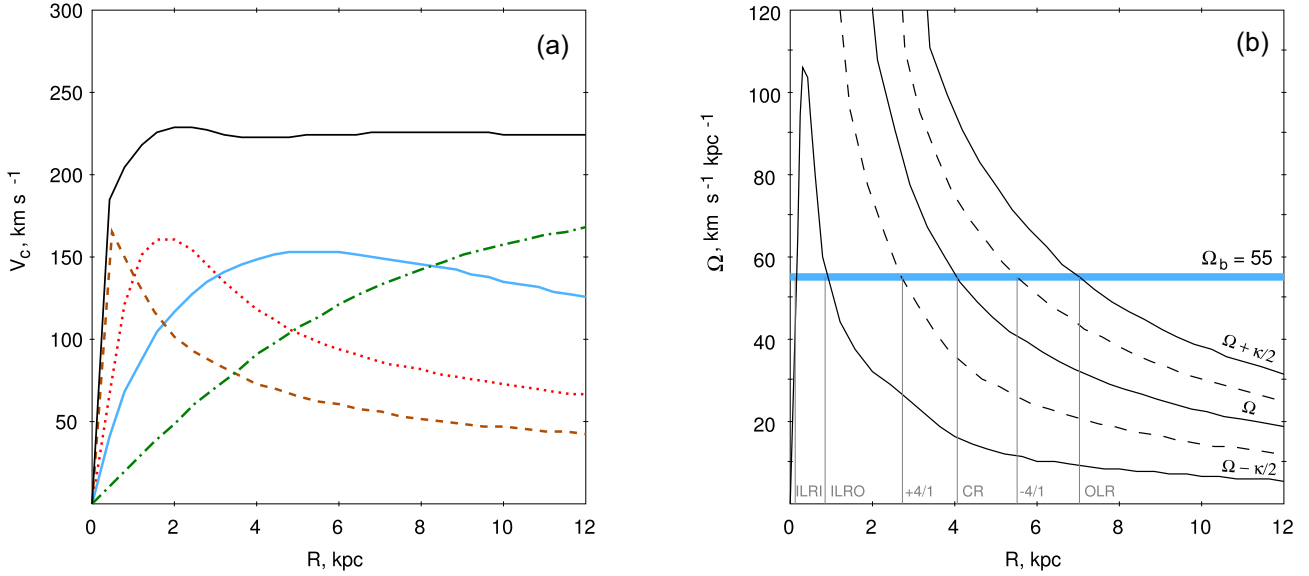


Figure 3. (a) Model rotation curve. The total rotation curve (the black curve) and the contribution of the bulge, bar, disc, and halo (the brown, red, blue, and green curves, respectively) to the rotation curve. (b) Dependence of the angular velocities Ω , $\Omega \pm \kappa/2$ (the solid curves) and $\Omega \pm \kappa/4$ (the dashed curves) on the distance R . The horizontal straight line (coloured in blue) indicates the angular velocity of the bar and its intersections with the curves of angular velocities mark the locations of the resonances.

Table 2. Model parameters.

Simulation time	$T = 3 \text{ Gyr}$
Step of integration	$\Delta t = 0.01 \text{ Myr}$
Number of particles	$N = 10^7$
Bulge	$R_{bg} = 0.30 \text{ kpc}$ $M_{bg} = 5 \cdot 10^9 M_{\odot}$
Bar	$a = 3.5$ and $b = 1.35 \text{ kpc}$ $M_b = 1.20 \cdot 10^{10} M_{\odot}$ $\Omega_b = 55.0 \text{ km s}^{-1} \text{ kpc}^{-1}$ $T_{gr} = 447 \text{ Myr}$
Disc	exponential, $R_d = 2.5 \text{ kpc}$ $M_d = 3.25 \cdot 10^{10} M_{\odot}$
Halo	$R_h = 8 \text{ kpc}$ $V_{max} = 201.4 \text{ km s}^{-1}$

Non-axisymmetric perturbations of the bar increase slowly approaching the full strength by $T_{gr} = 447 \text{ Myr}$, which is equal to four bar rotation periods. However, the $m = 0$ component of the bar is included in the model from the beginning. During the period of the bar growth, $0 < t < T_{gr}$, radial and azimuthal forces created by the bar were multiplied by the factor k_g which increases linearly from 0 to 1. We also introduce the additional force, f_a , which on the contrary decreases linearly with time:

$$\begin{cases} k_g = t/T_{gr} \\ f_a = (1 - k_g) \langle f_b \rangle < f_b \end{cases} \quad 0 < t < T_{gr}, \quad (14)$$

where $\langle f_b \rangle$ is the radial force created by the bar averaged over the azimuthal angle $\theta \in [0, 2\pi]$. The force $\langle f_b \rangle$ depends on the radius, R , so its values were tabulated before the simulation and then were calculated for a position of a particle by linear interpolation. This procedure ensures a constant average radial force at each radius during the bar-growth period. The $m = 0$ component of the bar can be interpreted as a pre-existent disc-like bulge (Athanasoula 2005).

The $q_t(R)$ quantity is often considered as the characteristic of perturbations created by a bar. It is calculated as the maximal ratio of the acceleration in the azimuthal direction to the average acceleration in the radial direction at a certain radius:

$$q_t(R) = \max \left(\frac{\max(|F_T|)}{\langle |F_R| \rangle} \right). \quad (15)$$

The strength of the bar, Q_b , is determined as the maximal value of q_t along the radius (Sanders & Tubbs 1980; Combes & Sanders 1981; Athanasoula et al. 1983). In the present model, the strength of the bar amounts to $Q_b = 0.3142$, which is a typical value for galaxies with strong bars (Block et al. 2001; Buta, Laurikainen & Salo 2004; Díaz-García et al. 2016).

The model of the Galaxy includes an exponential disc with a mass of $M_d = 3.25 \cdot 10^{10} M_{\odot}$ and a characteristic scale of $R_d = 2.5 \text{ kpc}$ (Bland-Hawthorn & Gerhard 2016). The total mass of the model disc and bar is $M_d + M_b = 4.45 \cdot 10^{10} M_{\odot}$, which agrees with other estimates of the Galactic-disc mass lying in the range $3.5\text{--}5.0 \cdot 10^{10} M_{\odot}$ (Shen et al. 2010; Fujii et al. 2019). The surface density of the disc is determined by the relation:

$$\Sigma = \Sigma_0 \exp^{-\frac{R}{R_D}}, \quad (16)$$

where Σ_0 is the density of the disc at the Galactic centre. Here we consider only the thin disc because the ratio of the surface densities of the thick and thin discs are supposed to be only 12 per cent at the solar distance (as a review Bland-Hawthorn & Gerhard 2016).

The classical bulge is modelled by a Plummer sphere with the mass of $M_{bg} = 5 \cdot 10^9$ (Dehnen & Binney 1998; Nataf 2017; Fujii et al. 2019). The halo is modelled by an isothermal sphere. More detailed description of the construction method for each Galactic subsystem is given in Melnik (2019).

3.2 The initial velocity distribution

We suppose that 3 Gyr ago the dependence of the radial velocity dispersion σ_R on the distance R in the $R = 5\text{--}11 \text{ kpc}$ interval was

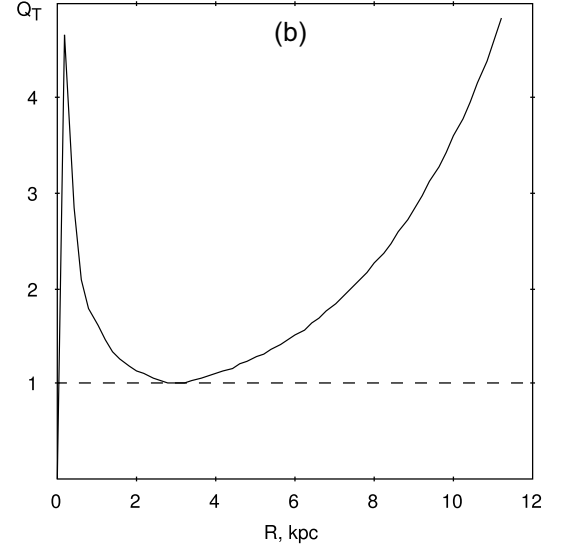
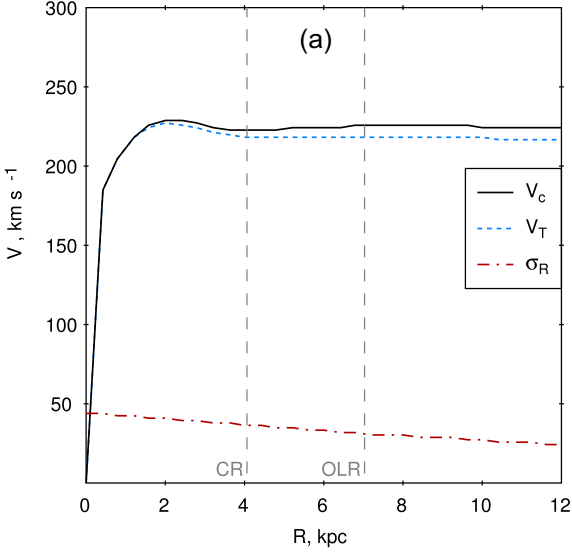


Figure 4. Initial velocity distribution of model particles. (a) Velocities of the rotation curve V_c (solid line), the average azimuthal velocities $\overline{V_T}$ (dashed line) and the initial velocity dispersion σ_R (dash-and-dot line) of model particles. (b) Dependence of the Toomre disc stability parameter Q_T on Galactocentric distance R built for the initial velocity distribution.

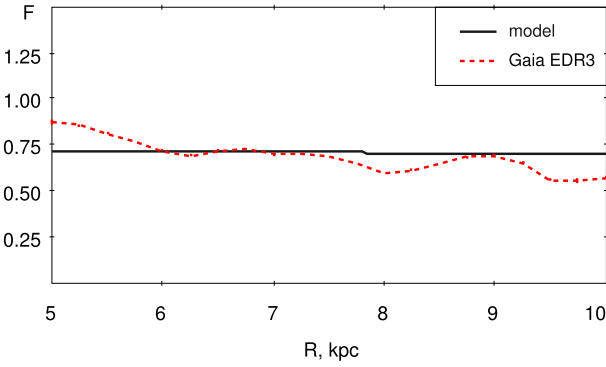


Figure 5. Dependence of the ratio of the observed velocity dispersions, σ_T/σ_R , derived from the *Gaia* EDR3 data (the red dashed line) and the model value $F = \kappa/(2\Omega)$ (the black line) on Galactocentric distance R . The value of F determines the ratio of the azimuthal and radial velocity dispersions adopted for the initial distribution of model particles.

similar to what is observed now:

$$\sigma_R = C_R^* \exp^{-\frac{R}{S_R}}, \quad (17)$$

where S_R is adopted to be $S_R = 20$ kpc (equation 9).

We want to make sure that the model disc is stable against axisymmetric perturbations at the initial time instant. So the value of the constant C_R^* is determined so as to ensure the Toomre stability parameter would be $Q_T \geq 1$ throughout the disc (Toomre 1964). In our model, Q_T achieves a minimum at the distance of $R = 3.1$ kpc, so the constant C_R^* is determined from the equation:

$$Q_T = \frac{\sigma_R \kappa}{3.36 G \Sigma} = 1 \quad (18)$$

at the distance of $R = 3.1$ kpc (Fig. 4b). This normalization yields the initial radial velocity dispersion at the solar distance of $\sigma_R = 30.5$ km s⁻¹, which is very close to the value of $\sigma_R = 31.5$ km s⁻¹ derived from the smooth distribution of the *Gaia* velocity dispersions (equation 9). After the model bar started growing, the velocity dispersion inside the

corotation radius ($R_{CR} = 4.0$ kpc) increased rapidly but we want the disc to be stable at the initial moment as well (see also Section 4.5).

Any subsystem of disc stars with a non-zero velocity dispersion rotates with a smaller average velocity than the velocity of the rotation curve (for example, Binney & Tremaine 2008). The relation between the average azimuthal velocity $\overline{V_T}$ and the velocity of the rotation curve V_c is determined by the Jeans equation:

$$\frac{\partial (\rho \overline{V_R^2})}{\partial R} + \frac{\partial (\rho \overline{V_R V_z})}{\partial z} + \rho \left(\frac{\overline{V_R^2} - \overline{V_T^2}}{R} + \frac{\partial \Phi}{\partial R} \right) = 0, \quad (19)$$

where ρ is the volume density of disc stars and Φ is the Galactic potential which is related to the velocity of the rotation curve by the following expression:

$$V_c^2 = R \frac{\partial \Phi}{\partial R}. \quad (20)$$

Assuming that the motions along coordinates R and z are independent, we can neglect the second term in the left part of equation (19). If we suppose that the distribution law along the coordinate z does not depend on the distance R , then we can substitute the volume density ρ for the surface density Σ . We assume that systematic motions are absent at the initial moment and can make following substitutions:

$$\overline{V_R^2} = \sigma_R^2, \quad (21)$$

$$\overline{V_T^2} = \overline{V_T^2} + \sigma_T^2, \quad (22)$$

which allows us to rewrite the Jeans equation in the following way:

$$\overline{V_T^2} = V_c^2 + \sigma_R^2 - \sigma_T^2 + \frac{R}{\Sigma} \frac{\partial (\Sigma \sigma_R^2)}{\partial R}. \quad (23)$$

Assuming the epicyclic approximation for the initial velocity distribution, we can write the following relation between the velocity dispersions along the radial and azimuthal directions:

$$\frac{\sigma_T}{\sigma_R} = \frac{\kappa}{2\Omega}. \quad (24)$$

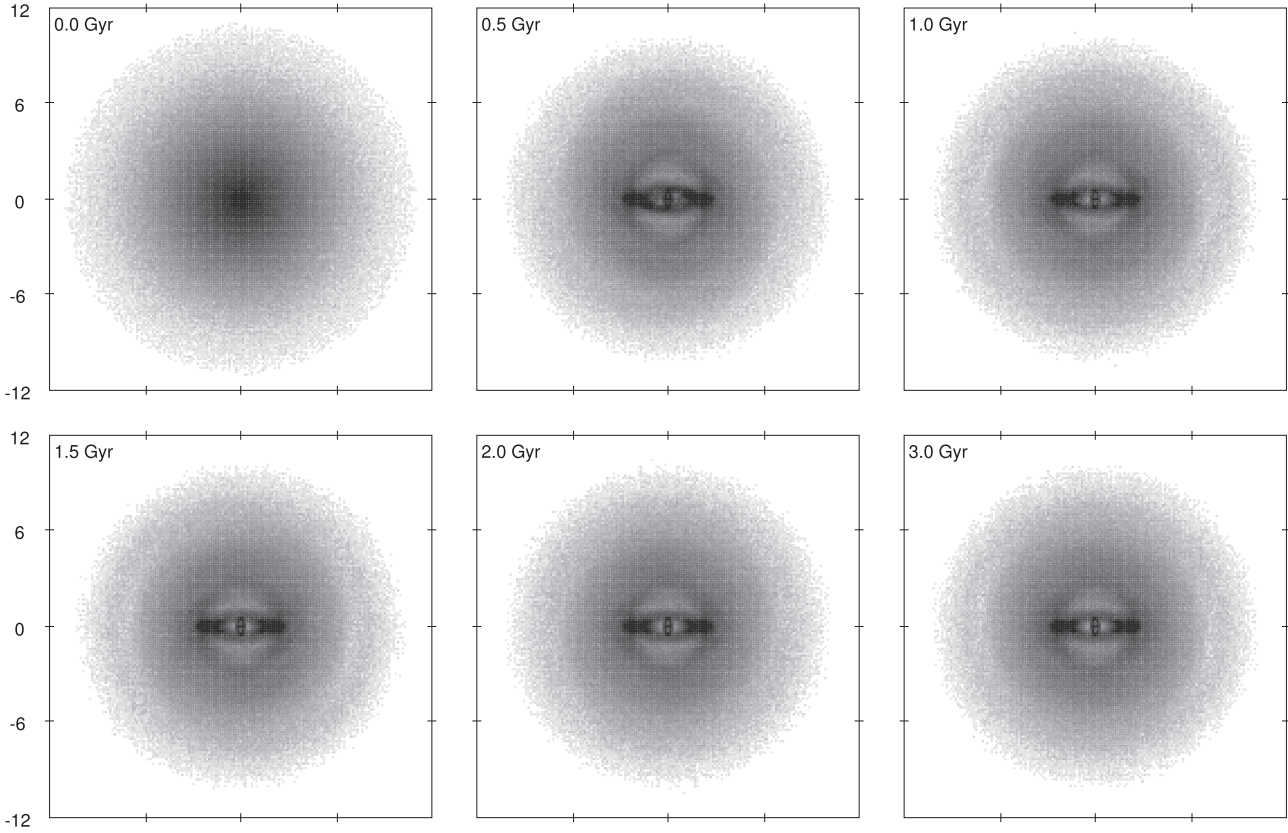


Figure 6. Distribution of the surface density of model particles in the Galactic disc at different time moments. The size of the frames is 24×24 kpc. The major axis of the bar is oriented horizontally. Two closest shades of grey correspond to a density change by a factor of 0.8. The model galaxy rotates counterclockwise.

We now use equations (9), (16), and (24) to obtain:

$$\overline{V_T}^2 = V_c^2 + \sigma_R^2 \left(1 - \frac{\kappa^2}{4\Omega^2} - \frac{R}{R_D} - \frac{2R}{S_R} \right), \quad (25)$$

where $\overline{V_T}$ is the average azimuthal velocity of model particles at the initial time instant.

Fig. 4(a) shows the distribution of the average azimuthal velocity, $\overline{V_T}$, of model particles along Galactocentric distance, R , at the initial instant. Also shown are the velocity of the rotation curve, V_c , and the radial velocity dispersion, σ_R , at the initial moment. We can see that the velocity $\overline{V_T}$ is always slightly lower than the velocity of the rotation curve and the difference $V_c - \overline{V_T}$ increases with the increasing distance R .

Fig. 5 shows the dependence of the ratio of the observed velocity dispersions of disc stars, σ_T/σ_R , and the model value $F = \kappa/(2\Omega)$ on Galactocentric distance R . The value of F determines the ratio of the azimuthal and radial velocity dispersions adopted for the initial distribution of model particles. We can see that F is almost constant and varies in the range $F = 0.70$ – 0.72 in the distance interval 5–10 kpc, which is quite expected for model with a flat rotation curve for which F must be equal to $F = 1/\sqrt{2}$. The formal errors in the determination of the observed ratio σ_T/σ_R are less than 0.01. The model value $F = \kappa/(2\Omega)$ is derived from the model potential so it is absolutely accurate. We can see that the *Gaia* EDR3 ratio of the velocity dispersions, σ_T/σ_R , decreases with increasing distance R , which can be due to the rapid change of the velocity dispersion σ_T with R (Table 1). However, in the solar neighbourhood of $|R - R_0| < 1.5$ kpc, the observed ratio σ_T/σ_R lies in the range 0.60–0.72. So here the model and observed values of the velocity dispersions are consistent to within 15 per cent.

4 RESULTS

4.1 Formation of the rings

The formation of elliptical resonance rings requires some time for the epicyclic motions of stars to adjust in accordance with the rotation of the bar. Fig. 6 shows the distribution of the surface density of model particles in the Galactic disc at different time instants. The time $t = 0$ corresponds to the instant when the bar is turned on. By the time $T_{gr} = 0.45$ Gyr the bar gains the full strength. One can see that the outer rings, R_1 and R_2 , are already formed by the time $t = 1$ Gyr. The ring R_1 is located closer to the Galactic centre and is stretched perpendicular to the bar so that the bar and ring R_1 are reminiscent of the Greek letter ‘ θ ’. The ring R_2 is located further away from the Galactic centre and is stretched parallel to the bar. Besides the outer rings, R_1 and R_2 , the Galactic disc produces the inner (r) and nuclear (n) resonance rings.

Fig. 7(a) shows the distribution of the surface density, Σ , of model particles along the distance R at different time moments. Local density minima between the following pairs of rings: n and r , r and R_1 , R_1 and R_2 , are immediately apparent. Interestingly, the location on the OLR precisely coincides with the density minimum.

Fig. 7(b) shows the distribution of the relative surface density, $\Delta\Sigma = \Sigma - \Sigma_0 + C$, of model particles near the OLR. The function Σ_0 describes the exponential density distribution at the start of the simulation but the constant $C = 3.2 \cdot 10^3 \text{ kpc}^{-2}$ is added to avoid dealing with negative values. We can see some variations in the width and density of the outer ring R_2 : at the times $t = 2.0$ and 3.0 Gyr the ring R_2 has larger width and smaller density than at the times $t = 1.5$ and 1.0 Gyr, which is mainly due to the shift of its inner

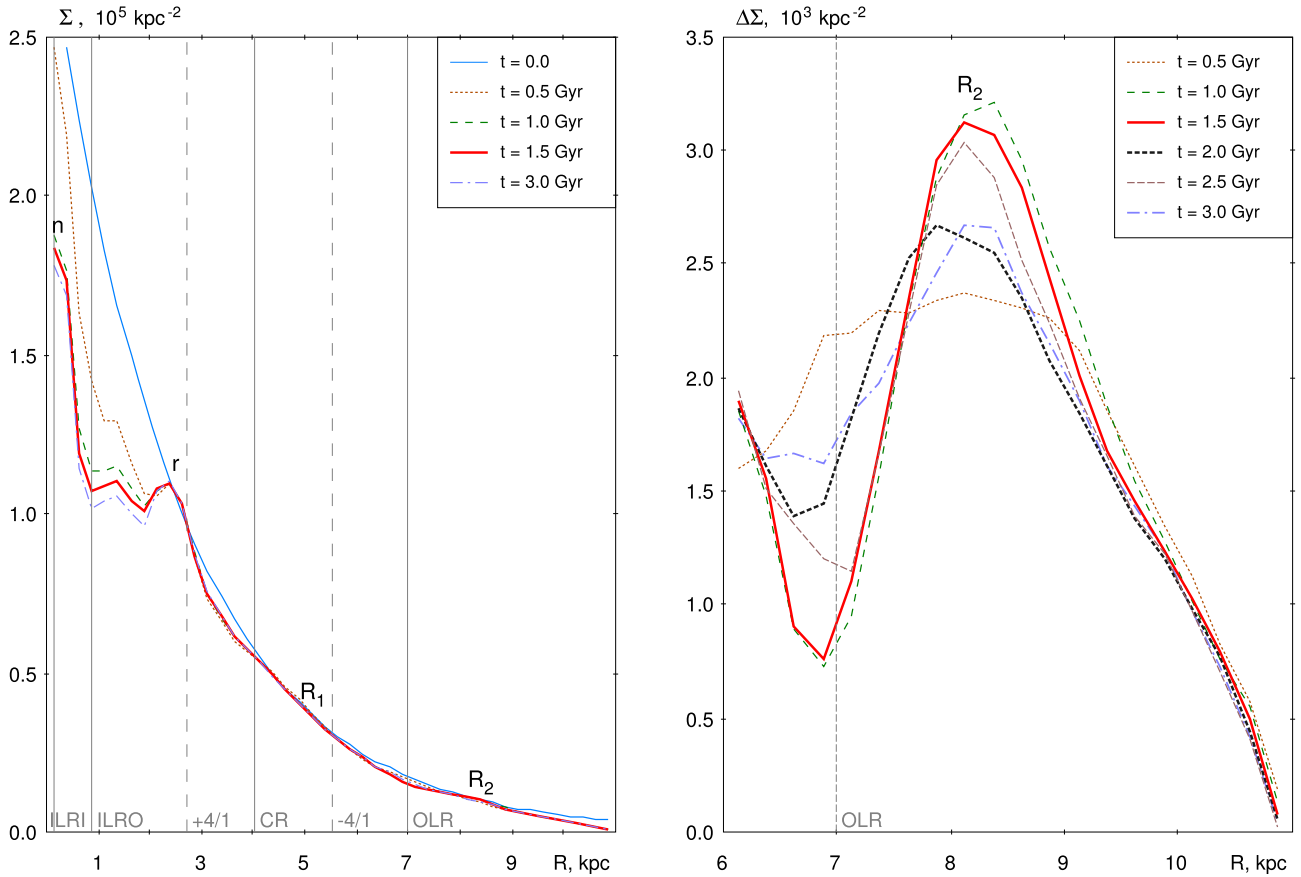


Figure 7. (a) Distribution of the surface density, Σ , of model particles along Galactocentric distance R at different time instants. The locations of the resonance rings are marked by the letters: n (nuclear ring), r (inner ring), R_1 and R_2 (outer rings). (b) Distribution of the relative surface density, $\Delta\Sigma = \Sigma - \Sigma_0 + C$, of model particles near the OLR, where Σ_0 is the initial exponential density distribution but the constant $C = 3.2 \cdot 10^3 \text{ kpc}^{-2}$ is added to avoid dealing with negative values. We can see some variations in the width and density of the outer ring R_2 : the ring R_2 has a flatter profile at the times $t = 2.0$ and 3.0 Gyr than at the times $t = 1.0$ and 1.5 Gyr.

boundary. Probably, here we see the periodically strengthening and weakening ring R_2 .

4.2 Comparison between the model and observed velocity profiles

Fig. 8 shows the model and observed dependence of the radial, V_R , and azimuthal, V_T , velocities of disc stars lying in the sector $|\theta| < 15^\circ$ on Galactocentric distance R . The model dependence are obtained for the angular velocity and the position angle of the bar equal to $\Omega_b = 55 \text{ km s}^{-1} \text{ kpc}^{-1}$ and $\theta_b = 45^\circ$, respectively. The position angle of the bar close to $\theta_b = 45^\circ$ is found in many studies (Hammersley et al. 2000; Benjamin et al. 2005; Cabrera-Lavers et al. 2007; Melnik & Rautiainen 2009; González-Fernández et al. 2012; Pettitt et al. 2014, and other papers). The median velocities of model particles were calculated in $\Delta R = 250$ -pc wide bins. Model velocity profiles were averaged over 0.5 Gyr time periods with a step of $\Delta t = 0.01$ Gyr. The random errors in the determination of the average model velocities in bins are smaller than 0.1 km s^{-1} . The observed velocity profiles were derived from the *Gaia* EDR3 data (section 2).

Fig. 8 (left-hand panel) shows the model and observed profiles of the radial velocity V_R . The model V_R profiles demonstrate a plateau in the distance interval $R = 5.0$ – 6.0 kpc, a smooth fall from the velocity $V_R = +5$ to -3 km s^{-1} over the interval $R = 6.0$ – 8.5 kpc

and a slow rise or a plateau with a constant negative velocity V_R in the interval $R = 8.5$ – 10.0 kpc. We can see that the model and observed V_R -profiles match well in the distance interval $R = 6$ – 9 kpc. Note that the model profiles of the velocity V_R obtained during the time periods $t = 0.5$ – 1.0 and 1.0 – 1.5 Gyr are steeper than the profiles calculated for the periods 1.5 – 2.0 , 2.0 – 2.5 , and 2.5 – 3.0 Gyr, which can result from a small increase in the velocity dispersion due to the tuning of the epicyclic motions near the OLR (i.e. to the formation of the outer rings). Generally, the model and observed V_R profiles match better during the time periods 1.5 – 2.0 , 2.0 – 2.5 , and 2.5 – 3.0 Gyr than at the times 0.5 – 1.0 and 1.0 – 1.5 Gyr.

Fig. 8 (right-hand panel) shows the model and observed profiles of the azimuthal velocity V_T . The model velocity V_T is almost constant, $V_T = 216$ – 218 km s^{-1} , at the start of the simulation (the slightly curved dashed line). The velocity V_T drops by 5 km s^{-1} at the distance of $R = 8.5$ kpc by the time $t = 1.0$ Gyr. We can see that the model and observed V_T profiles agree well over the distance interval $R = 6.0$ – 10.0 kpc at the time periods 1.0 – 1.5 and 1.5 – 2.0 Gyr. The model can reproduce the sharp drop of the velocities V_T in the distance interval $R = 7.5$ – 8.5 kpc just at the times 1.0 – 1.5 and 1.5 – 2.0 Gyr, but later the model velocity V_T demonstrates a smoother fall.

The study of the influence of the observational errors and selection effects on to the distributions of the velocities V_R and V_T along the distance R is presented in Appendix.

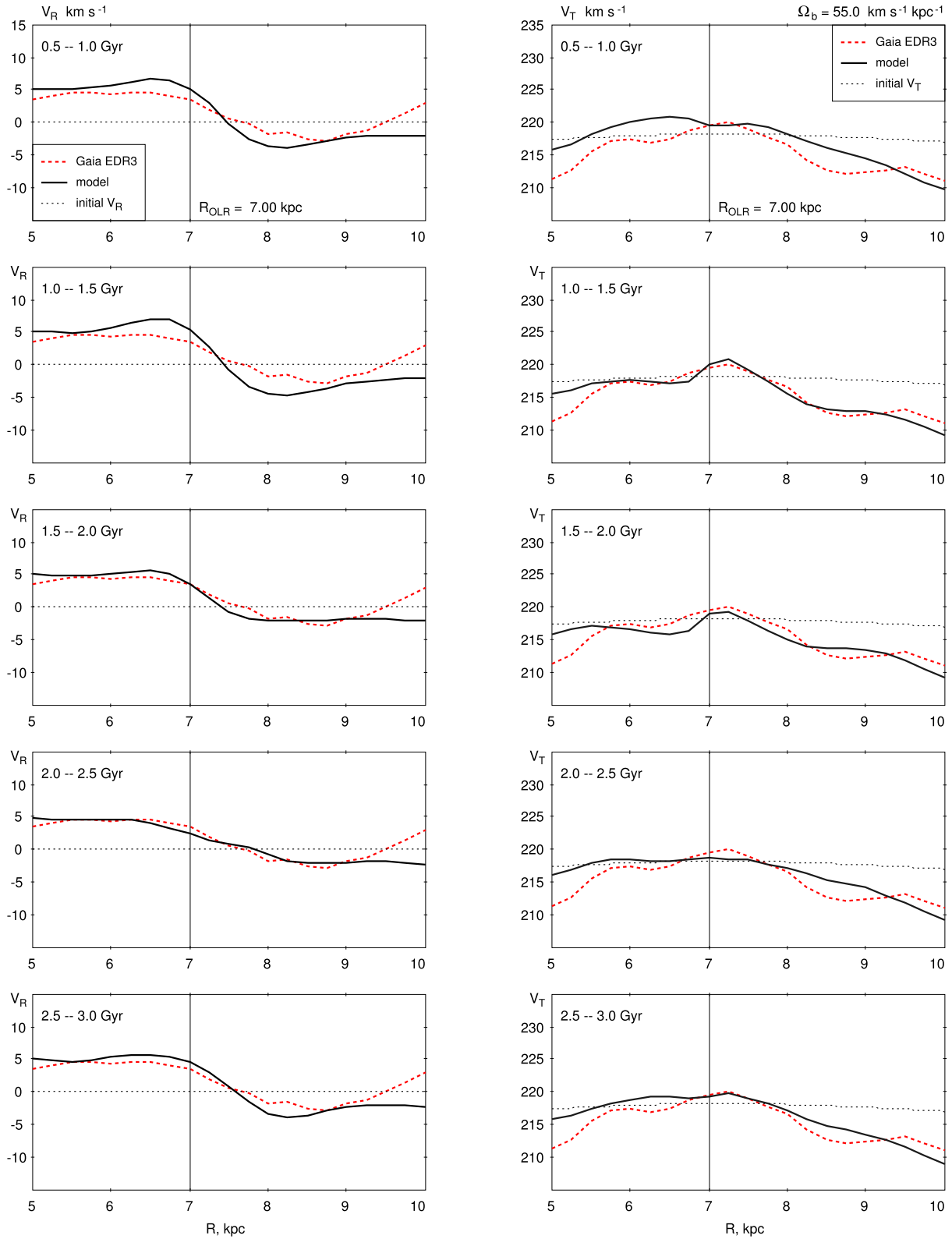


Figure 8. Model and observed dependence of the median radial and azimuthal velocities, V_R and V_T , of disc stars lying in the sector $|\theta| < 15^\circ$ on Galactocentric distance R . The model velocity profiles (the black curves) are obtained for the angular velocity and the position angle of the bar equal to $\Omega_b = 55 \text{ km s}^{-1} \text{ kpc}^{-1}$ and $\theta_b = 45^\circ$, respectively, and averaged over the time periods of 0.5 Gyr. The observed velocity profiles (the red dashed curves) are derived from the *Gaia* EDR3 data. The errors in determination of both *Gaia* EDR3 and model average velocities in bins are smaller than the line width. The dashed grey lines indicate the initial distribution of the velocities V_R and V_T . The boundaries of time periods are shown at each frame. The vertical lines indicate the location of the OLR.

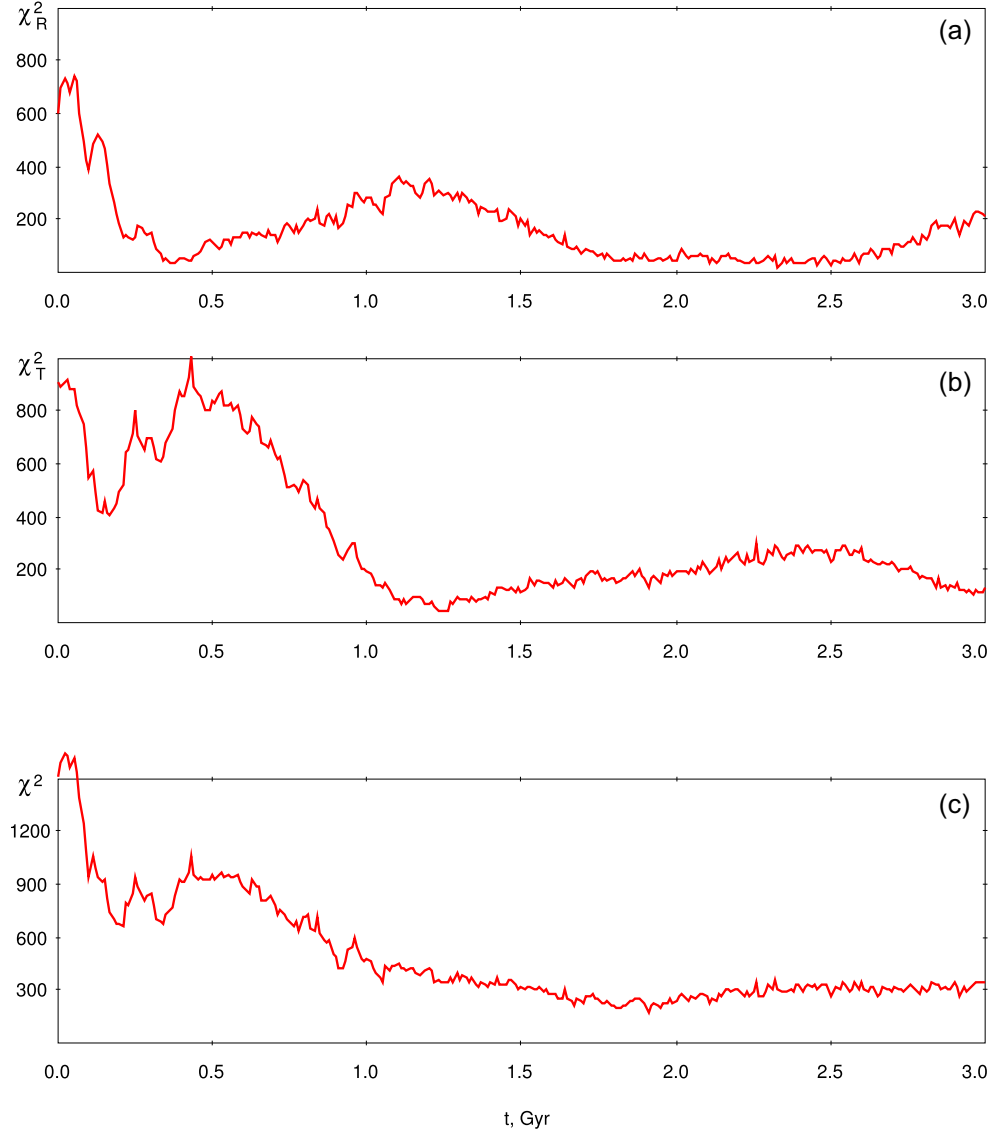


Figure 9. The functions χ_R^2 , χ_T^2 and their sum $\chi^2 = \chi_R^2 + \chi_T^2$. The χ^2 function reaches a minimum at the time 1.8 ± 0.5 Gyr.

4.3 Comparison of the velocity profiles during different time periods

We calculated the statistics χ^2 (the sum of squared differences between the model and observed velocities) to find the time periods during which the model and observed velocity profiles agree best. The values of χ_R^2 and χ_T^2 are computed in $n = 17$ bins in the distance interval $R = 5.5\text{--}9.5$ kpc for the radial and azimuthal velocity profiles, respectively:

$$\chi_R^2 = \sum^n \frac{(V_{R, \text{mod}} - V_{R, \text{obs}})^2}{\varepsilon_{VR}^2}, \quad (26)$$

$$\chi_T^2 = \sum^n \frac{(V_{T, \text{mod}} - V_{T, \text{obs}})^2}{\varepsilon_{VT}^2}, \quad (27)$$

where ε_{VR} and ε_{VT} are the average uncertainties in the determination of the model and observed velocities V_R and V_T in bins. The uncertainties in the determination of observational velocities V_R and instantaneous model velocities V_R (obtained without averaging over the time) are 0.2 and 0.3 km s⁻¹, so we adopted $\varepsilon_{VR} = 0.5$ km s⁻¹.

The uncertainties ε_{VR} and ε_{VT} are connected through the relation:

$$\varepsilon_{VT} = \frac{\kappa}{2\Omega} \varepsilon_{VR}, \quad (28)$$

where the coefficient $\kappa/(2\Omega)$ equals 0.71 in the interval $R = 5.5\text{--}9.5$ kpc (Fig. 5, black line).

Fig. 9 shows the variations in the values of χ_R^2 and χ_T^2 as well as in their sum $\chi^2 = \chi_R^2 + \chi_T^2$ with time t . A step in time is $\Delta t = 10$ Myr. We can see that the χ_R^2 , χ_T^2 , and χ^2 functions demonstrate small oscillations about the average values, which are due to the stochastic deviations of the velocities of model particles. The χ^2 function starts its decrease at $t = 0.5$ Gyr and reaches a plateau at the time 1 Gyr. The distribution of χ^2 in the time period 1–3 Gyr is not precisely flat but exhibits a shallow minimum at $t = 1.8$ Gyr. The location of the minimum is determined with the uncertainty of ± 0.5 Gyr corresponding to 1σ probability level.

It is just observational data derived from the *Gaia* EDR3 catalogue that produce the minimum at $t = 1.8 \pm 0.5$ Gyr. A comparison of our model with the velocity profiles derived from the *Gaia* DR2 catalogue does not yield a minimum at the time period 1–3 Gyr.

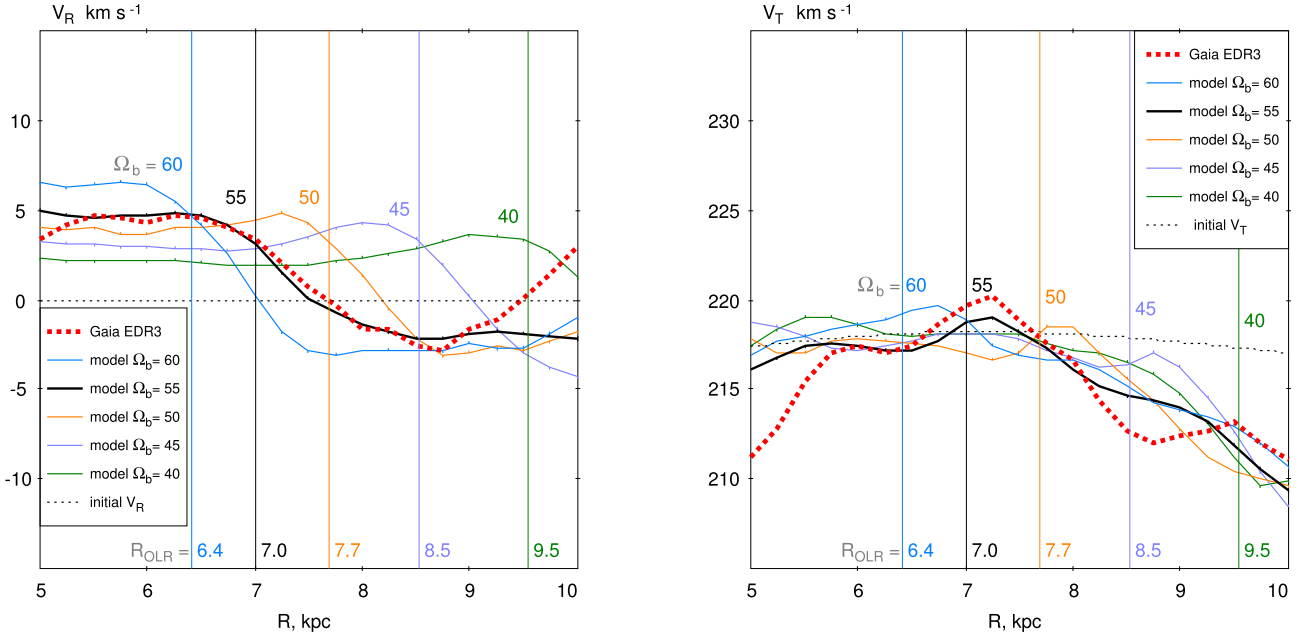


Figure 10. Model and observed distributions of the radial V_R (left-hand panel) and azimuthal V_T (right-hand panel) velocities along Galactocentric distance R . The model velocity profiles are calculated for the five values of the bar angular velocity: $\Omega_b = 40$ (green line), 45 (violet line), 50 (yellow line), 55 (thick black line), and 60 (blue line) $\text{km s}^{-1} \text{kpc}^{-1}$, and are averaged over the time period of $t = 1.5\text{--}2.0$ Gyr. The observed velocity profiles are derived from the *Gaia* EDR3 data (red dashed curves). The long vertical lines indicate the locations of the OLRs. The upper row of coloured numbers displays the values of Ω_b while the bottom row gives the values of R_{OLR} . The strokes on the curves indicate the random errors in the determination of the model median velocities in bins averaged over 50 profiles. The errors in the determination of the observed velocities in bins are comparable with the line width. We can see that the bar angular velocity of $\Omega_b = 55 \text{ km s}^{-1} \text{kpc}^{-1}$ provides the best agreement between the model and observed velocity profiles while the values of $\Omega_b = 40\text{--}50$ and $60 \text{ km s}^{-1} \text{kpc}^{-1}$ cause the model velocity profiles to be shifted towards larger and smaller distances R , respectively.

4.4 Comparison of the velocity profiles calculated for different values of Ω_b and θ_b

Fig. 10 shows the distributions of the radial and azimuthal velocities, V_R and V_T , along Galactocentric distance R calculated for five values of the bar angular velocity: $\Omega_b = 40, 45, 55,$ and $60 \text{ km s}^{-1} \text{kpc}^{-1}$. The position angle of the bar is supposed to be $\theta_b = 45^\circ$. Model velocity profiles are averaged for the time period of $t = 1.5\text{--}2.0$ Gyr. We can see that the value of the bar angular velocity equal to $\Omega_b = 55 \text{ km s}^{-1} \text{kpc}^{-1}$ provides the best agreement between the model and observed V_R - and V_T -velocity profiles. Note, that the model velocity profiles computed, on the one hand, for the speeds of $\Omega_b = 40, 45, 50 \text{ km s}^{-1} \text{kpc}^{-1}$ and, on the other hand, for $60 \text{ km s}^{-1} \text{kpc}^{-1}$ are shifted with respect to the observed profiles towards larger and smaller distances R , respectively. The larger the bar angular velocity Ω_b , the smaller the radius of the OLR. Fig. 10 also shows that the radial velocity V_R starts decreasing nearly at the radius of the OLR while the azimuthal velocity V_T demonstrates a slight rise just at the distance of the OLR and starts its drop only at the distance exceeding the radius of the OLR by nearly 0.7 kpc : $R \sim R_{\text{OLR}} + 0.7 \text{ kpc}$.

Fig. 11(a) shows variations in the χ^2 values averaged over the time periods $t = 1.0\text{--}1.5, 1.5\text{--}2.0,$ and $2.5\text{--}3.0$ Gyr as a function of the bar angular velocity Ω_b . The vertical lines indicate the dispersions of the χ^2 values. We can see that the χ^2 functions achieve minima at $\Omega_b = 55 \text{ km s}^{-1} \text{kpc}^{-1}$. The 1σ confidence interval calculated for the time period $1.5\text{--}2.0$ Gyr is $52\text{--}57 \text{ km s}^{-1} \text{kpc}^{-1}$. The function χ^2 computed for the time period $1.5\text{--}2.0$ Gyr achieves smaller values than χ^2 obtained for other periods but the difference is close to 1σ .

The value of the bar angular velocity of $\Omega_b = 55 \text{ km s}^{-1} \text{kpc}^{-1}$ corresponds to the location of the OLR of the bar at $R_{\text{OLR}} = 7.00 \text{ kpc}$. The adopted value of the solar Galactocentric distance is $R_0 =$

7.5 kpc , so the radius of the OLR must be shifted by 0.5 kpc towards the Galactic centre with respect to the solar circle. The uncertainty in the values of Ω_b , $52\text{--}57 \text{ km s}^{-1} \text{kpc}^{-1}$, produces the uncertainty in the radius of the OLR equal to $6.75\text{--}7.40 \text{ kpc}$ and the shift of the OLR with respect to the solar circle is determined with the uncertainty $R_{\text{OLR}} = R_0 - 0.5^{+0.4}_{-0.3} \text{ kpc}$.

The position angle of the bar, θ_b , is the angle between the direction of the bar major axis and the Sun–Galactic centre line. Fig. 11(b) shows variations in the χ^2 values averaged over the time periods $t = 1.0\text{--}1.5, 1.5\text{--}2.0,$ and $2.5\text{--}3.0$ Gyr with the position angle θ_b . We can see that the χ^2 function built for the time period $1.5\text{--}2.0$ Gyr demonstrates a sharp drop at the interval $0\text{--}30^\circ$ followed by a plateau with a shallow minimum at $\sim 45^\circ$. The 1σ confidence interval for the location of the minimum is $\theta_b = 25\text{--}60^\circ$.

4.5 Comparison between the model and observed velocity dispersions

Fig. 12 shows variations in the dispersions of the radial, σ_R , and azimuthal, σ_T , velocities with the distance R calculated for the model and observed velocities. The model σ_R - and σ_T -profiles are plotted with the time-step of $\Delta t = 0.2 \text{ Gyr}$. We can see that the model velocity dispersions, σ_R and σ_T , demonstrate a fast growth inside the corotation radius $R < 4.0 \text{ kpc}$ during the first 0.6 Gyr , after which changes become very small. But beyond this radius, $R > 4.0 \text{ kpc}$, the velocity dispersions change only slightly during the entire simulation time. However, we can notice a small growth of the radial velocity dispersion, σ_R , near the OLR: from the initial value of $\sigma_R = 31.6 \text{ km s}^{-1}$ ($t = 0$) to maximum of 34.7 km s^{-1} at $t = 1.3 \text{ Gyr}$ and then back to 32.8 km s^{-1} at $t = 2.5 \text{ Gyr}$. Probably, such small up-and-down

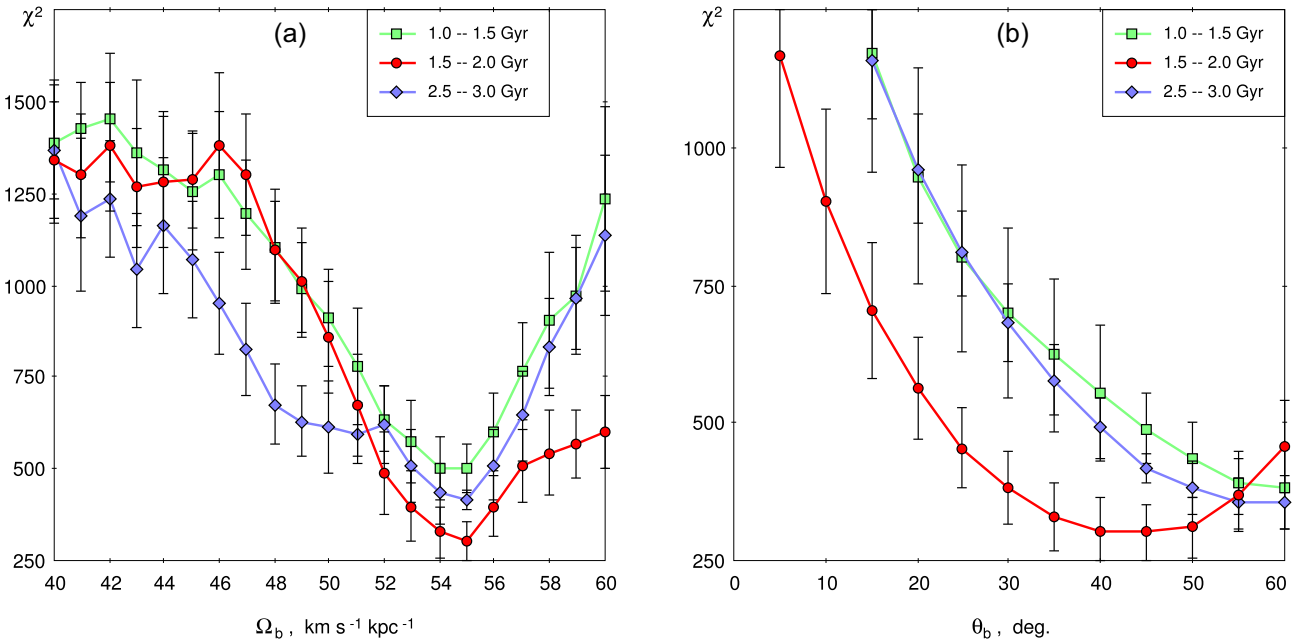


Figure 11. Variations in the χ^2 values averaged over the time periods $t = 1.0\text{--}1.5$, $1.5\text{--}2.0$ and $2.5\text{--}3.0$ Gyr (a) along the angular velocity of the bar, Ω_b , and (b) along the position angle of the bar, θ_b . The vertical lines indicate the dispersions of the χ^2 values. The χ^2 function calculated for the time period $1.5\text{--}2.0$ Gyr achieves smaller values than χ^2 obtained for other time periods but the difference is close to 1σ . (a) The minima of the χ^2 functions correspond to the value of $\Omega_b = 55 \text{ km s}^{-1} \text{ kpc}^{-1}$. The 1σ confidence interval calculated for the time period $1.5\text{--}2.0$ Gyr is $\Omega_b = 52\text{--}57 \text{ km s}^{-1} \text{ kpc}^{-1}$. (b) The χ^2 function built for the time period $1.5\text{--}2.0$ Gyr demonstrates a sharp drop at the interval $0\text{--}30^\circ$ followed by a plateau with a shallow minimum at $\sim 45^\circ$. The 1σ confidence interval for the location of the minimum is $\theta_b = 25\text{--}60^\circ$.

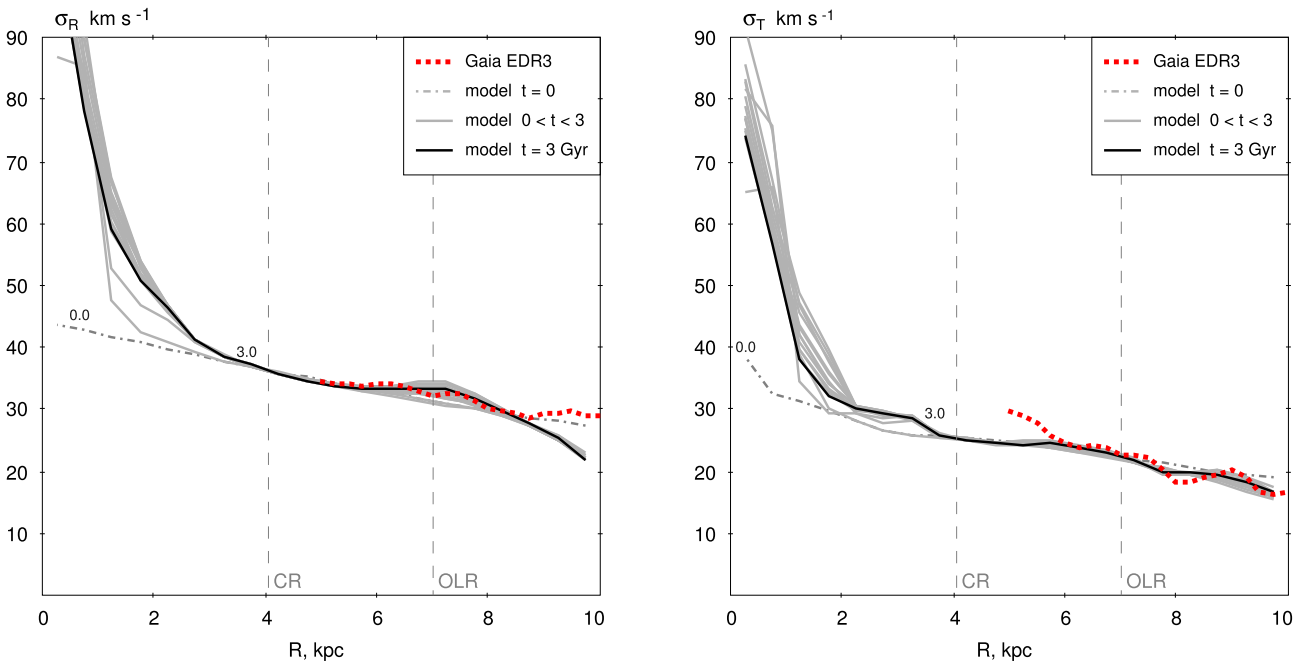


Figure 12. Variations in the radial, σ_R , and azimuthal, σ_T , velocity dispersions as a function of Galactocentric distance R obtained for the model (black and grey curves) and observed (red dashed curves) velocities. The model profiles of the velocity dispersions are plotted with the time-step of $\Delta t = 0.2$ Gyr. The model velocity dispersions demonstrate a fast increase inside the corotation radius $R < 4.0$ kpc during the first 0.6 Gyr after which changes are very small. But beyond this radius, $R > 4.0$ kpc, the velocity dispersions change only slightly during the entire simulation time. However, we can notice a small growth of the radial velocity dispersion, σ_R , near the OLR. The model and observed velocity dispersions agree to within ~ 15 per cent in the distance interval $R = 6\text{--}9$ kpc.

changes are due to the tuning of orbits near the resonance rings R_1 and R_2 (see discussion in Melnik 2019). Generally, the model and observed velocity dispersions agree to within ~ 15 percent in the distance interval $R = 6\text{--}9$ kpc.

5 DISCUSSION AND CONCLUSIONS

The *Gaia* catalogue mainly includes F-G-K type stars of the main sequence of the Hertzsprung–Russell diagram (Gaia Collaboration 2018b) among which there are stars of different ages. Large spectroscopic surveys such as SDSS/APOGEE (Majewski et al. 2017), LAMOST (Zhao et al. 2012), and GALAH (De Silva et al. 2015) give an opportunity to obtain massive estimates of ages of red stars in the Galaxy. The median ages of stars located in the Galactic-midplane at the solar distance appear to lie in the range 2–7 Gyr. In addition, the average age of disc stars increases towards the Galactic centre (Ness et al. 2016; Frankel et al. 2019; Wu et al. 2019). The decrease of stellar ages in the outer part of the Galactic disc is often thought to be due to a gas accretion episode at a look-back time of 5–9 Gyr (Spitoni et al. 2019; Lian et al. 2020). Another explanation is connected with the emergence of the bar and the formation of the outer resonance rings near the solar circle, which stimulates the movement of gas from the outer disc to the solar neighbourhood (Haywood et al. 2019).

We selected stars from the *Gaia* EDR3 catalogue with reliable parallaxes, proper motions, and line-of-sight velocities located near the Galactic plane, $|z| < 200$ pc, and in the sector of the Galactocentric angles $|\theta| < 15^\circ$. For each 250-pc wide Galactocentric distance bin, we calculated the median velocities in the radial and azimuthal directions, V_R and V_T . The observed distributions of the velocities over the Galactocentric distance, R , have some specific features: the radial velocity, V_R , demonstrates a smooth decrease from $+5$ km s^{-1} at the distance of $R \approx R_0 - 1.5$ kpc to -3 km s^{-1} at $R \approx R_0 + 1.0$ kpc while the azimuthal velocity, V_T , shows a sharp drop by 7 km s^{-1} in the distance interval $R_0 < R < R_0 + 1.0$ kpc.

The observed dispersion of radial velocities, σ_R , at the solar distance R_0 is equal to $\sigma_R = 31.5$ km s^{-1} . The velocity dispersion σ_R increases in the direction of the Galactic centre and its variations in the distance interval $R = 5\text{--}11$ kpc can be approximated by the exponential law with a scale length of 22 ± 2 kpc.

We built a model of the Galaxy including bulge, bar, disc, and halo components, which reproduces the observed specific features of the velocity profiles in the Galactocentric distance interval $|R - R_0| < 1.5$ kpc. The best agreement between the model and observed velocity profiles corresponds to the time $t = 1.8 \pm 0.5$ Gyr after the start of the simulation.

The model of the Galaxy with the bar rotating at the angular velocity of $\Omega_b = 55$ km s^{-1} kpc $^{-1}$ provides the best agreement between the model and observed velocity profiles. The value of $\Omega_b = 55$ km s^{-1} kpc $^{-1}$ sets the OLR of the bar at the distance of $R_{\text{OLR}} = R_0 - 0.5$ kpc. The 1σ confidence interval for the values of Ω_b is $\Omega_b = 52\text{--}57$ km s^{-1} kpc $^{-1}$ which corresponds to the uncertainty in the OLR location of $\sim \pm 0.4$ kpc.

The position angle of the bar, θ_b , with respect to the Sun corresponding to the best agreement between the model and observed velocities is $\theta_b = 45^\circ$. The 1σ confidence interval amounts to $25\text{--}60^\circ$.

ACKNOWLEDGEMENTS

We thank the anonymous referee and the editor for useful remarks and suggestions. We also thank E. V. Glushkova for the discussion.

This work has made use of data from the European Space Agency (ESA) mission *Gaia* (<https://www.cosmos.esa.int/gaia>), processed by the *Gaia* Data Processing and Analysis Consortium (DPAC, <https://www.cosmos.esa.int/web/gaia/dpac/consortium>). Funding for the DPAC has been provided by national institutions, in particular the institutions participating in the *Gaia* Multilateral Agreement. AD acknowledges the support from the Russian Foundation for Basic Research (project no. 19-02-00611).

DATA AVAILABILITY

The data underlying this article were derived from sources in the public domain: VizieR at <https://vizier.u-strasbg.fr/viz-bin/VizieR>.

REFERENCES

- Arenou F. et al., 2018, *A&A*, 616, 17
 Asano T., Fujii M. S., Baba J., Bédorf J., Sellentin E., Portegies Zwart S., 2020, *MNRAS*, 499, 2416
 Athanassoula E., 1992, *MNRAS*, 259, 328
 Athanassoula E., 2005, *MNRAS*, 358, 1477
 Athanassoula E., Bienayme O., Martinet L., Pfenniger D., 1983, *A&A*, 127, 349
 Athanassoula E., Romero-Gómez M., Masdemont J. J., 2009, *MNRAS*, 394, 67
 Baba J., Kawata D., 2020, *MNRAS*, 492, 4500
 Benjamin R. A. et al., 2005, *ApJ*, 630, L149
 Bensby T. et al., 2017, *A&A*, 605, A89
 Bernard E. J., Schultheis M., Di Matteo P., Hill V., Haywood M., Calamida A., 2018, *MNRAS*, 477, 3507
 Binney J., Tremaine S., 2008, *Galactic Dynamics*, Second Edition. Princeton Univ. Press, Princeton, New Jersey
 Bland-Hawthorn J., Gerhard O., 2016, *ARA&A*, 54, 529
 Block D. L. et al., 2001, *A&A*, 375, 761
 Boehle A. et al., 2016, *ApJ*, 830, 17
 Branham R. L., 2017, *Ap&SS*, 362, 29
 Buta R., 1995, *ApJS*, 96, 39
 Buta R., Combes F., 1996, *Fundam. Cosm. Phys.*, 17, 95
 Buta R., Crocker D. A., 1991, *AJ*, 102, 1715
 Buta R., Laurikainen E., Salo H., 2004, *AJ*, 127, 279
 Byrd G., Rautiainen P., Salo H., Buta R., Crocker D. A., 1994, *AJ*, 108, 476
 Cabrera-Lavers A. et al., 2007, *A&A*, 465, 825
 Carrillo I. et al., 2019, *MNRAS*, 490, 797
 Chiba R., Friske J. K. S., Schonrich R., 2021, *MNRAS*, 500, 4710
 Churchwell E. et al., 2009, *PASP*, 121, 213
 Combes F., Sanders R. H., 1981, *A&A*, 96, 164
 Comerón S. et al., 2014, *A&A*, 562, 121
 Contopoulos G., Grosbøl P., 1989, *A&AR*, 1, 261
 Contopoulos G., Papayannopoulos Th., 1980, *A&A*, 92, 33
 Dambis A. K., Berdnikov L. N., Kniazev A. Y., Kravtsov V. V., Rastorguev A. S., Sefako R., Vozyakova O. V., 2013, *MNRAS*, 435, 3206
 De Silva G. M. et al., 2015, *MNRAS*, 449, 2604
 Debattista V. P., Sellwood J. A., 2000, *ApJ*, 543, 704
 Debattista V. P. et al., 2019, *MNRAS*, 485, 5073
 Dehnen W., 2000, *AJ*, 119, 800
 Dehnen W., Binney J., 1998, *MNRAS*, 294, 429
 Díaz-García S., Salo H., Laurikainen E., Herrera-Endoqui M., 2016, *A&A*, 587, 160
 Dwek E. et al., 1995, *ApJ*, 445, 716
 Efremov Yu. N., Sitnik T. G., 1988, *Sov. Astron. Lett.*, 14, 347
 Eilers A.-Ch., Hogg D. W., Rix H.-W., Ness M. K., 2019, *ApJ*, 871, 120
 Eskridge P. B. et al., 2000, *AJ*, 119, 536
 Feast M. W., Laney C. D., Kinman T. D., van Leeuwen F., Whitelock P. A., 2008, *MNRAS*, 386, 2115
 Fragkoudi F. et al., 2019, *MNRAS*, 488, 3324

- Francis Ch., Anderson E., 2014, *MNRAS*, 441, 1105
- Frankel N., Sanders J., Rix H.-W., Ting Y.-S., Ness M., 2019, *ApJ*, 884, 99
- Freeman K. C., 1970, *ApJ*, 160, 811
- Fujii M. S., Bédorf J., Baba J., Portegies Zwart S., 2019, *MNRAS*, 482, 1983
- Fux R., 2001, *A&A*, 373, 511
- Gaia Collaboration, 2016, *A&A*, 595, A1
- Gaia Collaboration, 2018a, *A&A*, 616, A1
- Gaia Collaboration, 2018b, *A&A*, 616, A10
- Gaia Collaboration, 2018c, *A&A*, 616, A11
- Gaia Collaboration, 2021, *A&A*, 650, C3
- Gerhard O., 2011, Mem. S. A. It. Suppl., 18, 185
- Glushkova E. V., Dambis A. K., Melnik A. M., Rastorguev A. S., 1998, *A&A*, 329, 514
- González-Fernández C., López-Corredoira M., Amôres E. B., Minniti D., Lucas P., Toledo I., 2012, *A&A*, 546, 107
- Groenewegen M. A. T., Udalski A., Bono G., 2008, *A&A*, 481, 441
- Hammersley P. L., Garzon F., Mahoney T. J., Lopez-Corredoira M., Torres M. A., 2000, *MNRAS*, 317, L45
- Hasselquist S., 2020, *ApJ*, 901, 109
- Haywood M., Di Matteo P., Snaith O., Calamida A., 2016, *A&A*, 593, A82
- Haywood M., Snaith O., Lehnert M. D., Di Matteo P., Khoperskov S., 2019, *A&A*, 625, A105
- Kalnajs A. J., 1991, in Sundelius B., ed., Dynamics of Disc Galaxies. Göteborgs Univ., Göteborg, p. 323
- Katz D. et al., 2019, *A&A*, 622, A205
- Kormendy J., Kennicutt R. C., 2004, *ARA&A*, 42, 603
- Leung H. W., Bovy J., 2019, *MNRAS*, 489, 2079
- Li Z., Shen J., 2012, *ApJ*, 757, L7
- Lian J. et al., 2020, *MNRAS*, 494, 2561
- Lindgren L. et al., 2018, *A&A*, 616, A2
- Lindgren L. et al., 2021, *A&A*, 649, A2
- Majewski S. R. et al., 2017, *AJ*, 154, 94
- Marshall D. J., Robin A. C., Reyle C., Schultheis M., Picaud S., 2006, *A&A*, 453, 635
- Melnik A. M., 2019, *MNRAS*, 485, 2106
- Melnik A. M., Dambis A. K., 2020, *Ap&SS*, 365, 112
- Melnik A. M., Rautiainen P., 2009, *Astron. Lett.*, 35, 609
- Melnik A. M., Rautiainen P., 2011, *MNRAS*, 418, 2508
- Melnik A. M., Rautiainen P., Berdnikov L. N., Dambis A. K., Rastorguev A. S., 2015, *AN*, 336, 70
- Melnik A. M., Rautiainen P., Glushkova E. V., Dambis A. K., 2016, *Ap&SS*, 361, 60
- Melvin T., Masters K., the Galaxy Zoo Team, 2013, Memorie della Societa Astronomica Italiana Supplement, 25, 82
- Menéndez-Delmestre K., Sheth K., Schinnerer E., Jarrett T., Scoville N. Z., 2007, *ApJ*, 657, 790
- Nataf D. M., 2016, *PASA*, 33, 23
- Nataf D. M., 2017, *PASA*, 34, 41
- Neckel Th., Klare G., 1980, *ApJS*, 42, 251
- Ness M., Lang D., 2016, *AJ*, 152, 14
- Ness M., Hogg D. W., Rix H.-W., Martig M., Pinsonneault M. H., Ho A. Y. Q., 2016, *ApJ*, 823, 114
- Nikiforov I. I., 2004, in Byrd G. G., Kholshchevnikov K. V., Myllari A. A., Nikiforov I. I., Orlov V. V., eds, ASP Conf. Ser. Vol. 316, Structure and Kinematics of the Milky Way Galaxy. Astron. Soc. Pac., San Francisco, p. 199
- Pettitt A. R., Dobbs C. L., Acreman D. M., Price D. J., 2014, *MNRAS*, 444, 919
- Pfenniger D., 1984, *A&A*, 134, 373
- Pohl M., Englmaier P., Bissantz N., 2008, *ApJ*, 677, 283
- Rautiainen P., Melnik A. M., 2010, *A&A*, 519, 70
- Rautiainen P., Salo H., 1999, *A&A*, 348, 737
- Rautiainen P., Salo H., 2000, *A&A*, 362, 465
- Rautiainen P., Salo H., Laurikainen E., 2008, *MNRAS*, 388, 1803
- Reid M. J., Menten K. M., Zheng X. W., Brunthaler A., Xu Y., 2009, *ApJ*, 705, 1548
- Riess A. G., Casertano S., Yuan W., Macri L. M., Scolnic D., 2018, *ApJ*, 861, 126
- Rodriguez-Fernandez N. J., Combes F., 2008, *A&A*, 489, 115
- Sanders R. H., Tubbs A. D., 1980, *ApJ*, 235, 803
- Sanders J. L., Smith L., Evans N. W., 2019, *MNRAS*, 488, 4552
- Sartoretti P. et al., 2018, *A&A*, 616, A6
- Schönrich R., McMillan P., Eyer L., 2019, *MNRAS*, 487, 3568
- Schwarz M. P., 1981, *ApJ*, 247, 77
- Sellwood J. A., Wilkinson A., 1993, *Rep. on Prog. in Phys.*, 56, 173
- Shen J., Rich R. M., Kormendy J., Howard C. D., Propris R. D., Kunder A., 2010, *ApJ*, 720, L72
- Sheth K. et al., 2008, *ApJ*, 675, 1141
- Simion I. T., Belokurov V., Irwin M., Kposov S. E., Gonzalez-Fernandez C., Robin A. C., Shen J., Li Z.-Y., 2017, *MNRAS*, 471, 4323
- Sormani M. C., Sobacchi E., Fragkoudi F., Ridley M., Treß R. G., Glover S. C. O., Klessen R. S., 2018, *MNRAS*, 481, 2
- Spitoni E., Aguirre V. S., Matteucci F., Calura F., Grisoni V., 2019, *A&A*, 623, A60
- Toomre A., 1964, *ApJ*, 139, 1217
- Trick W. H., Fragkoudi F., Hunt J. A. S., Mackereth J. T., White S. D. M., 2021, *MNRAS*, 500, 2645
- Wu Y. et al., 2019, *MNRAS*, 484, 5315
- Yalyaliev L. N., Chemel A. A., Glushkova E. V., Dambis A. K., Klinichev A. D., 2018, *Astrophys. Bull.*, 73, 335
- Zhao G., Zhao Y.-H., Chu Y.-Q., Jing Y.-P., Deng L.-C., 2012, *Res. Astron. Astrophys.*, 12, 723
- Zinn J. C., Pinsonneault M. H., Huber D., Stello D., 2019, *ApJ*, 878, 136

APPENDIX

We studied the effect of observational errors on to the distribution of the velocities V_R and V_T along Galactocentric distance R derived from *Gaia* EDR3 data. Generally, the selection effects together with errors in parallax can create some bias between the true and observational velocities. To simulate observational errors, we created the spacial distribution of model particles close to the observed distribution, and added normally distributed errors to the true values of parallaxes, proper motions, and line-of sight velocities. The standard deviations of model errors in parallaxes ($\sigma_\varpi = 0.016$ mas), proper motions ($\sigma_\mu = 0.015$ mas yr⁻¹), and line-of-sight velocities ($\sigma_{v_r} = 2.0$ km s⁻¹) are supposed to be equal to the average values of errors given in the *Gaia* DR3 catalogue for the sample of stars considered: $|\theta| < 15^\circ$, $|z| < 200$ pc, $5 < R < 10$ kpc.

Figs A1(a) and (b) show the distribution of the median velocities V_R and V_T calculated in $\Delta R = 250$ -pc wide bins for the true values of ϖ , μ , and V_r and for the values affected by observational errors. We can see that observational errors have practically no effect on the velocity profiles calculated in bins at least at the distance range $R = 5$ –10 kpc. The average difference between the velocities calculated for the true and observed data is 0.1 km s⁻¹ which is comparable to the random errors.

Fig. A1(c) and (d) describes the method of modelling the observational distribution. Fig. A1(c) shows the spacial distributions of model particles, n , in bins normalized to the number of particles, n_0 , in the bin centred at the solar position ($R_0 = 7.5$ kpc) calculated for the exponential disc (f_{mod}) and for *Gaia* DR3 stars (f_{obs}). We can see that the logarithmic distribution of model particles in the exponential disc (f_{mod}) is close to the straight line while the distribution of *Gaia* DR3 stars in our sample is bell-like-shaped (see also Fig. 1b). To mimic the selection effect, we retained all model particles in the bin centred at the solar position and only a small fraction of particles in the bins located far from the solar circle.

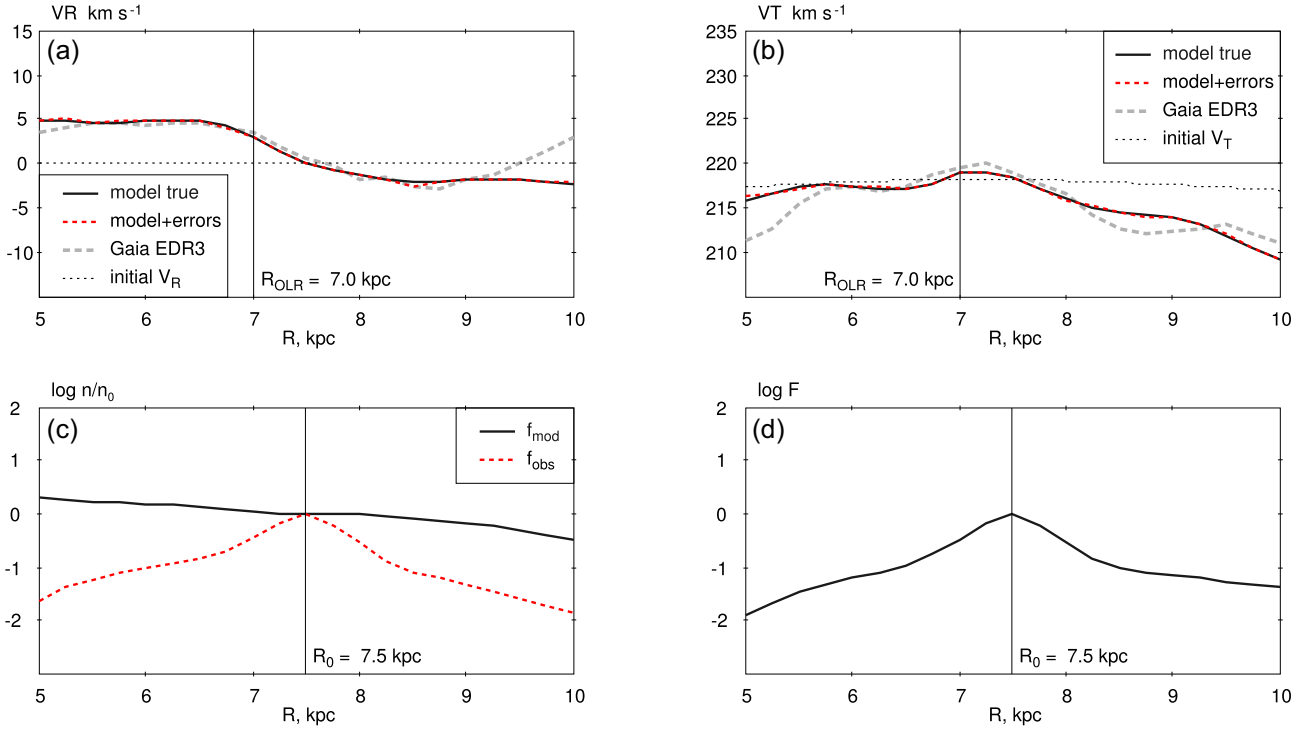


Figure A1. (a) and (b) Influence of observational errors on the distribution of the velocities V_R (a) and V_T (b) along the distance R . The black solid lines describe the true velocity profiles of model particles calculated in bins ($|\theta| < 15^\circ$, $|z| < 200$ pc, $\Delta R = 250$ pc) while the red dashed lines indicate the velocity profiles of model particles affected by random errors in parallaxes ($\sigma_\varpi = 0.016$ mas), proper motions ($\sigma_\mu = 0.015$ mas yr⁻¹) and line-of-sight velocities ($\sigma_{v_r} = 2.0$ km s⁻¹). We can see that observational errors have practically no effect on the velocity profiles in the distance interval $R = 5$ –10 kpc. Also shown are the velocity profiles computed for *Gaia* DR3 stars. (c) and (d) To study the effect of observational errors we simulated the spacial distribution of model particles close to the observed distribution. (c) Spacial distributions of model particles, n , in bins obtained for exponential discs (f_{mod}) and for *Gaia* DR3 stars (f_{obs}) normalized at the number of particles, n_0 , located at the bin centred at the solar position ($R_0 = 7.5$ kpc). (d) Function $F = f_{\text{mod}}/f_{\text{obs}}$ indicates the fraction of model particles which must be retained in each bin to mimic the selection effects in the distribution of *Gaia* DR3 stars with known line-of-sight velocities. Functions f_{mod} , f_{obs} , and F are presented in logarithmic form.

Fig. A1(d) shows the fraction, $F = f_{\text{mod}}/f_{\text{obs}}$, of model particles which must be retained in each bin to mimic the selection effect in the distribution of *Gaia* DR3 stars with known line-of-sight velocities (Sartoretti et al. 2018; Katz et al. 2019). Function F equals unity, $F = 1$, at the solar position and it is less than 0.1, $F < 0.1$, in the bins located farther than 1 kpc from the solar circle, $|R - R_0| > 1$ kpc. The asymmetry of function F with respect to the solar position means

that we should exclude more particles in the direction towards the Galactic centre than in the opposite direction.

Thus, we can neglect the observational errors in our analysis of the velocity distributions along the distance R .

This paper has been typeset from a \LaTeX file prepared by the author.